

A whole-planet model of the Earth without life for terrestrial exoplanet studies

SAMANTHA GILBERT-JANIZEK ,¹ RORY K. BARNES ,¹ PETER E. DRISCOLL ,² NICHOLAS F. WOGAN ,^{3,4}
 AVI M. MANDELL ,^{5,6} JESSICA L. BIRKY ,⁷ LUDMILA CARONE ,⁸ AND RODOLFO GARCIA¹

¹Department of Astronomy and Astrobiology Program, University of Washington, Box 351580, Seattle, Washington 98195

²Earth and Planets Laboratory, Carnegie Institution for Science, Washington, DC 20015, USA

³SETI Institute, Mountain View, CA 94043

⁴NASA Ames Research Center, Moffett Field, CA 94035

⁵NASA Goddard Space Flight Center, 8800 Greenbelt Road, Greenbelt, MD 20771, USA

⁶Sellers Exoplanet Environment Collaboration, 8800 Greenbelt Road, Greenbelt, MD 20771, USA

⁷Astronomy Department, University of Washington, Seattle, WA 98195, USA

⁸Space Research Institute, Austrian Academy of Sciences, Schmiedlstrasse 6, A-8042 Graz, Austria

ABSTRACT

As the only known habitable (and inhabited) planet in the universe, Earth informs our search for life elsewhere. Future telescopes like the Habitable Worlds Observatory (HWO) will soon look for life on rocky worlds around Sun-like stars, so it is critical that we understand how to distinguish habitable planets from inhabited planets. However, it remains unknown if life is necessary to maintain a habitable planet, or how all of the components of an evolving planet impact habitability over time. To address these open questions, we present a coupled interior-atmosphere evolution model of the Earth without life from 50 Myr to 5 Gyr that reproduces 19 key observations of the pre-industrial Earth within measurement uncertainties after 4.5 Gyr. We also produce a reflected light spectrum covering the possible wavelength range of HWO. Our findings support the view that life is not required to maintain habitable surface conditions. The model presented here is apt for predicting the long-term habitability of Earth-like exoplanets via evolving bulk properties. By generating realistic reflected light spectra from evolved atmospheric states, this model represents significant progress towards whole-planet modeling, which may ultimately provide a robust abiotic baseline for interpreting biosignature observations with HWO.

1. INTRODUCTION

Earth is currently the only known inhabited planet in the universe, and geological evidence suggests that it was habitable with liquid water oceans for most of its 4.54 Gyr history (Cameron et al. 2024). Owing to its long-term habitability, Earth serves as the template that guides our search for biospheres elsewhere. Consequently, a validated model of the entire planet is valuable for both understanding our own planet and optimizing the search for life on worlds outside the Solar System. To assist in these types of investigations, here we present a coupled one-dimensional core-mantle-crust-climate model of the Earth that reproduces 17 of 19 key observations of the pre-industrial Earth within $1-\sigma$ of

measurement uncertainties, and 2 observations of pre-industrial ocean carbonate chemistry within $2-\sigma$.

An open question regarding Earth’s evolution is whether or not it could be habitable without life’s influence on the environment. The idea that life plays an active role in maintaining conditions favorable to its survival is popularly known as the “Gaia hypothesis” (Lovelock & Margulis 1974). The Gaia hypothesis thus begs the question: is life *required* to maintain a habitable planet?

We will address this question by simulating the Earth through time without life with the goal of reproducing the habitable conditions of the pre-industrial Earth after 4.5 Gyr. Ultimately, whether or not life is a requirement for habitability has vast implications for the search for life on exoplanets; if life is not required for habitability, then the detection of habitable conditions alone is insufficient evidence for life. Instead, distinguishing inhabited from habitable and uninhabited worlds will re-

quire identifying atmospheric gases or surface features that can only be produced by life.

Developing this capability is critical as next-generation telescopes like the Habitable Worlds Observatory (HWO) prepare to search for life on nearby exoplanets. HWO is a space-based, infrared/optical/ultraviolet direct imaging telescope of 6 meters or larger that will discover and characterize Earth-like planets around Sun-like stars (National Academies of Sciences, Engineering, and Medicine 2021; Mamajek & Stapelfeldt 2023; Feinberg et al. 2026). The proper interpretation of photometry and spectroscopy of the pale dots detected in the habitable zone (HZ) of nearby stars with HWO is predicated on a complete and self-consistent model of Earth-like planets, defined as rocky planets with approximately Earth’s mass and radius (Wolf et al. 2017) and active interior-atmosphere volatile exchange (Rodler & López-Morales 2014; Fan et al. 2019). This broad definition likely includes planets with diverse compositions (Shim 2014; Santerne et al. 2018), atmospheric structures (Vladilo et al. 2013), stellar hosts (Mamajek & Stapelfeldt 2023), instellations (Kopparapu et al. 2013), and even habitable planets that never developed life (Cockell 2014; Wordsworth & Pierrehumbert 2014; López-Morales et al. 2019; Krissansen-Totton et al. 2021). The atmospheres of “abiotic Earths” must be well-quantified to serve as null hypotheses for identifying life’s signatures and ruling out its imitators, or “false positives”, on exoplanets observed with HWO (Meadows et al. 2018; Krissansen-Totton et al. 2021).

Many studies have simulated the co-evolution of the Earth and Sun based on geological evidence (Barley et al. 2005; Kharecha et al. 2005; Zerkle et al. 2012; Charnay et al. 2013; Arney et al. 2016; Krissansen-Totton et al. 2018; Catling & Zahnle 2020; Wogan et al. 2022) and extrapolated these results to predict the conditions of Earth-like planets around other stars (Segura et al. 2005; Kaltenegger et al. 2007; Segura et al. 2010; Frank et al. 2014; Godolt et al. 2015, 2016; Arney et al. 2017; Gebauer et al. 2017; Wolf et al. 2017; Rugheimer & Kaltenegger 2018; Arney 2019; Young et al. 2023). The existing work largely models the atmospheric evolution of these systems by coupling climate to photochemistry to achieve atmospheric compositions that are in radiative-convective equilibrium. However, atmospheric evolution cannot be fully understood in isolation from interior processes that regulate volatile cycling through the crust and mantle. While some studies have explored atmospheric evolution coupled to the mantle (Krissansen-Totton et al. 2021), to our knowledge no previous study has modeled the abiotic Earth by cou-

pling a core-mantle-crust-climate model to an evolving Sun. To correctly interpret HWO spectra of Earth-like planets, we must close this gap by developing a “whole planet” model that co-evolves the core, mantle, crust, atmosphere, and star (Foley & Driscoll 2016).

Here we present a one-dimensional, core-mantle-crust-climate model of the abiotic Earth that tracks the evolution of the core-mantle system, geochemistry, atmosphere, incoming solar flux, and solar effective temperature over the age of the Solar System. We use our model to reproduce 19 observed quantities of the pre-industrial Earth. We choose this calibration point as the modern Earth is not in radiative balance due to human-driven climate change. Due to large uncertainties in early Earth conditions, we do not attempt to validate the model on the conditions of the early Earth. Finally, as a proof of concept, we demonstrate that atmospheric states from our model can be used to generate realistic reflected light spectra comparable to observations HWO will obtain of Earth-like exoplanets.

For the remainder of this introduction, we describe the observed properties of the pre-industrial Earth and review previous work modeling its evolution. We describe the whole planet abiotic Earth model in Section 2, and present its validated results in Section 3. We discuss future model upgrades as well as potential applications of our validated model for HWO observations of Earth-like exoplanets in Section 4. Finally, we summarize our results and conclusions in Section 5.

1.1. Properties of the Pre-Industrial Earth

In this subsection, we discuss the known properties of the pre-industrial Earth (PIE). The “pre-industrial” era defines the period of Earth’s history prior to the industrial revolution (c. 1800), when widespread changes to human land-use and atmospheric pollution first arose (Hawkins et al. 2017). From records, geological evidence, and modeling reconstructions, the PIE is known to have had lower atmospheric and ocean CO₂ concentrations and cooler global average surface temperatures than today. Measurements of these properties with their uncertainties and corresponding sources are summarized in Table 1. We report interior properties based on present-day measurements because (1) pre-industrial measurements of these properties are largely nonexistent, and (2) mantle and core properties evolve on a sufficiently slow timescale that any variation from their present-day values should be insignificant. Similarly, we assume that the total mass of the ocean has not varied significantly in the last 300 years.

1.1.1. Atmosphere

Table 1. Selected properties of the pre-industrial Earth.

Property	Value	Reference(s)
Atmosphere		
Atmospheric CO ₂ ($p\text{CO}_2$)	$28.4 \pm 0.4 \text{ Pa}$	(1)
Atmospheric H ₂ O ($p\text{H}_2\text{O}$)	$900 \pm 700 \text{ Pa}$	(2, 3)
Global avg. surface temperature (T_{surf})	$286.9 \pm 0.1 \text{ K}$	(4, 5)
Surface		
Ground albedo (A_g)	0.14 ± 0.02	(6, 7, 8)
Ocean mass (w_{ocean})	$1.4 \times 10^{21} \text{ kg}$ (1 T.O.)	(9)
Oceanic (CO ₂) _{aq}	$8 \pm 2 \mu\text{mol/kg}$	(10)
Surface Ocean Total Dissolved Inorganic Carbon (DIC)	$2000 \pm 200 \mu\text{mol/kg}$	(10, 11)
Ocean pH	8.18 ± 0.05	(12)
Interior		
Upper mantle temperature (T_{UM})	$1587_{-34}^{+164} \text{ K}$	(13)
Core-mantle boundary temp. (T_{CMB})	$4000 \pm 200 \text{ K}$	(14)
Upper mantle heat flow (Q_{UM})	$38 \pm 3 \text{ TW}$	(13)
Core-mantle boundary heat flow (Q_{CMB})	$11 \pm 6 \text{ TW}$	(13)
Upper mantle viscosity (ν_{UM})	$(2.275 \pm 2.27) \times 10^{18} \text{ m}^2 \text{ s}^{-1}$	(15)
Lower mantle viscosity (ν_{LM})	$(1.5 \pm 1.4) \times 10^{18} \text{ m}^2 \text{ s}^{-1}$	(15)
Upper mantle melt fraction (f_{UM})	$11.5 \pm 3.5\%$	(16)
Mantle melt mass flux	$(1.3 \pm 0.8) \times 10^6 \text{ kg/s}$	(17, 18)
Inner core radius (R_{IC})	$1224.1 \pm 0.1 \text{ km}$	(13)
Magnetic moment	$80 \pm 4 \text{ ZAm}^2$ ($1.00 \pm 0.05 \text{ E.U.}$)	(19, 20)
Magnetopause radius	$9.10 \pm 0.14 \text{ R}_{\oplus}$ ($1.00 \pm 0.02 \text{ E.U.}$)	(21)

References: (1) Etheridge et al. (1996), (2) Robinson et al. (2011), (3) Lustig-Yaeger et al. (2023), (4) Hawkins & Sutton (2016), (5) Hawkins et al. (2017), (6) Solomon et al. (2007), (7) Kargel et al. (2014), (8) Genda (2016), (9) Charette & Smith (2010), (10) Feely et al. (2001), (11) Eide et al. (2017), (12) Jiang et al. (2019), (13) Jaupart et al. (2015), (14) Hirose et al. (2013), (15) Paulson et al. (2005), (16) Gale et al. (2013), (17) Cogné & Humler (2004), (18) Li et al. (2015), (19) de Pater & Lissauer (2010), (20) Kivelson & Bagenal (2014), (21) Driscoll & Bercovici (2013).

Earth retains a 1-bar atmosphere consisting of 78% N₂ (United States Committee on Extension to the Standard Atmosphere 1976). Oxygen, which comprises 21% of our atmosphere, became a major constituent after the proliferation of photosynthetic life (Kump 2008; Farquhar et al. 2011; Lyons et al. 2014). The remaining atmosphere consists of “trace components”, including CO₂ and H₂O, which are effective greenhouse gases that help regulate planetary climate (Tyndall 1861). Water vapor is the most efficient greenhouse gas (Fleming 1998), and because warmer air can hold more water vapor, the atmospheric abundance of H₂O relates to global temperature in a positive feedback loop (Held & Soden 2000;

Patel & Kuttippurath 2023). Below we detail measurements of Earth’s atmospheric CO₂ and H₂O abundances, as well as global average surface temperature. We also discuss recent measurements of atmospheric escape to space.

A record of atmospheric CO₂ levels has been pieced together by analyzing air trapped in polar ice sheets. Etheridge et al. (1996) analyzed air bubbles in Antarctic ice cores dating back to 1000 C.E., finding that pre-industrial atmospheric CO₂ abundances were around 280 ppm with annual fluctuations of ~ 4 ppm. In Earth’s 1-bar atmosphere (101325 Pa), this abundance is equivalent to a partial pressure of $28.4 \pm 0.4 \text{ Pa}$.

The abundance of H_2O in our atmosphere varies with latitude, with higher abundances in the humid tropics (Mockler 1995; Allan et al. 2022), as well as altitude, with higher abundances below the atmospheric cold trap (Brewer 1949; Randel & Park 2019). The abundance and distribution of water vapor is also seasonally variable, but the resulting change to the global atmosphere is small, on the order of $\pm 1 \times 10^{15}$ kg H_2O , or less than 0.02% of the total atmospheric mass (Trenberth et al. 1987). Satellite and sounding measurements have provided anchor points for 1-D models to map the vertical distribution of water vapor throughout Earth’s atmosphere; for example, Robinson et al. (2011) analyzed archived satellite data corresponding to the dates of the EPOXI Earth-flyby mission in 2008, extracting water vapor abundance profiles at latitudes of 0° , 19° , 41° , and 66° (Lustig-Yaeger et al. 2023, their Fig. 4). Each latitude profile represents the globally averaged vertical profile for all HEALPix bins with the corresponding north and south latitudes. The mean water vapor profile includes a near-surface water vapor volume mixing ratio of 0.0089, with near-surface abundances of 0.0158 and 0.00182 for the mean profiles acquired at 0° and 66° , respectively (Lustig-Yaeger et al. 2023). Treating the equatorial and mid-latitude averages as upper and lower bounds, these measurements correspond to a present-day partial pressure of 900 ± 700 Pa, a large uncertainty that reflects the strong latitude-dependency of near-surface water vapor abundances.

Earth’s global average surface temperature can be traced through time directly via historical records, and indirectly by estimating evolving radiative forcings, using global climate model simulations, and finally by compiling proxy evidence from tree-rings, corals, and ice cores. Hawkins et al. (2017) combine all of these approaches to estimate that pre-industrial temperatures were $0.55\text{--}0.80^\circ\text{C}$ cooler than the global average surface temperature from 1986 to 2005. Establishing the corresponding 1986-2005 baseline as 14.4°C (Hawkins & Sutton 2016), we therefore assume the pre-industrial global average surface temperature to be 286.9 ± 0.1 K (Hawkins et al. 2017).

Earth’s atmosphere is slowly leaking into space. Today, hydrogen – the lightest element – is most vulnerable to escape. Satellite measurements reveal that Earth is losing 12×10^{26} neutral H atoms per second via Jeans escape and charge exchange escape (Tian et al. 2013; Gronoff et al. 2020), and approximately 8×10^{25} ionized H^+ ions per second via magnetized ion outflow (Gunell et al. 2018; Gronoff et al. 2020). Thus, the present-day rate of hydrogen escape is a slow “trickle”, primarily because key hydrogen-bearing species like CH_4 and H_2O

rarely reach the upper atmosphere – most tropospheric CH_4 oxidizes into CO_2 and H_2O , and most of our atmospheric water vapor inventory is kept close to the surface by the cold trap (Gronoff et al. 2020). Notably, isotopic fractionation of noble gases like xenon suggests that atmospheric escape may have been more powerful in Earth’s past when the solar XUV flux was higher, potentially driving helium loss (Zahnle et al. 2019) and permanently oxidizing our atmosphere (Catling et al. 2001). Furthermore, predictive models suggest that when the Sun brightens by 10% in 1 Gyr, hydrogen escape will effectively desiccate Earth’s surface and leave small habitable oases only at the poles (Kasting 1988; Catling & Zahnle 2009). Given the slow escape rates, we assume Earth is not losing significant atmospheric loss.

1.1.2. Surface Properties

To first order, Earth’s surface includes exposed land, oceans, and polar ice caps. These three surface types, along with atmospheric water vapor clouds, contribute to the overall brightness or surface albedo of the planet, regulating planetary absorption of stellar radiation. In addition to H_2O , the oceans comprise dissolved inorganic carbon (DIC) in the form of aqueous CO_2 , carbonate (CO_3^{2-}), and bicarbonate (HCO_3^-), which together mediate the overall pH of the marine environment.

Earth sustains a surface liquid water ocean of mass 1.4×10^{21} kg, or by definition, 1 terrestrial ocean (T.O.) (Charette & Smith 2010). Earth’s vast oceans are a major carbon sequestration reservoir. Atmospheric CO_2 dissolves into the oceans as aqueous CO_2 and reacts with water to form carbonic acid, which dissociates into H^+ and HCO_3^- , which itself dissociates into H^+ and CO_3^{2-} (Pilson 2012).

Studies of ocean carbon isotopic fractionation reveal that the pre-industrial oceanic carbon budget is largely abiotic. Since photosynthetic respiration preferentially uses the ^{12}C isotope (O’Leary 1981), ocean water enriched in heavier ^{13}C indicates abiotic dissolved inorganic carbon (Quay et al. 2003). Isotopic fractionation studies suggest non-human biological activity accounts for only $\sim 2\%$ of the total DIC in the oceans (Carroll et al. 2022). Though marine life pumps dissolved carbon from the near-surface water column to the deep ocean (Le Moigne 2019), gravitational sinking dominates carbon export in modern oceans (Boyd et al. 2019; Nowicki et al. 2022; Siegel et al. 2023). Recent work using models to reconstruct pre-industrial ocean chemistry supports near-surface, pre-industrial DIC concentrations of $2000 \pm 200 \mu\text{mol/kg}$ (Feely et al. 2001; Eide et al. 2017), an aqueous CO_2 concentration of $8 \pm 2 \mu\text{mol/kg}$ (Feely

et al. 2001), and a global average surface ocean pH of 8.18 ± 0.05 (Jiang et al. 2019).

Planetary surface albedo, a linear combination of albedo contributions from different surface types and clouds, affects climate by regulating the Earth's absorbed shortwave radiation from the Sun. Based on data from spectral libraries (Jet Propulsion Laboratory 1999; Clark et al. 2003), previous planetary modeling work assumes that the albedo of seawater, rock, and ice are largely wavelength independent (Kaltenegger et al. 2007; Driscoll & Bercovici 2013), where ocean albedo $A_{oc} = 0.1$, rock albedo $A_r = 0.17$, and ice albedo $A_i = 0.6$. The ocean covers 71% of Earth's surface area (Genda 2016), and the remainder comprises land with seasonal variations in ice coverage. Satellite measurements have been used to quantify a perennial surface ice area of $16.01 - 16.04 \times 10^6 \text{ km}^2$ (Solomon et al. 2007; Kargel et al. 2014), or a perennial ice surface fraction of 3.4% that implies a remaining ice-free land surface fraction of 25.6%. On Earth, most of the ice-less land is covered by vegetation (Chu 2019), with 54% grasslands ($A \sim 0.4$) and 30% forests ($A \sim 0.1$). Since we are investigating an abiotic planet without life of any kind, we will assume that the surface of the abiotic Earth would instead be dominated by rock. Calculating the total expected ground albedo (A_g) as a linear combination of surface fraction and albedo contributions, we thus calculate $A_g = 0.14$. Seasonal changes in Earth's albedo imply variations of ± 0.02 (Bartman 1980).

In reality, Earth's *total* albedo also receives major contributions from atmospheric water vapor clouds, as satellite measurements suggest Earth's total albedo is closer to $A_T = 0.29$ (Wielicki et al. 1996; Loeb et al. 2009). This total albedo is ~ 0.15 brighter than the composite ground albedo because clouds are highly reflective, and they partially block the path of stellar radiation to the ground (Ramanathan et al. 1989; Harrison et al. 1990). For an albedo representing an average of thick and thin clouds, de Pater & Lissauer (2010) and Driscoll & Bercovici (2013) use $A_{cl} = 0.89$.

1.1.3. *Interior*

Beneath a thin crustal layer, Earth has a convecting solid mantle, molten outer core, and solid iron inner core. Here we describe how various measurements and models have been used to establish values (with uncertainties) for key core and mantle properties of the Earth, including temperature, heat flow, viscosity, upper mantle melt fraction, and magnetic moment.

The mantle geotherm describes how the laterally-averaged temperature of the mantle changes with depth. The temperature of the mantle at various depths may

be estimated using petrological constraints on the temperature of mid-ocean ridge basalts (Kinzel & Grove 1992) and the identification of several important phase changes: the 440 km deep olivine-wadsleyite phase change (Katsura et al. 2004), the 660 km deep post-spinel phase transition, (Katsura et al. 2003), and the inner core boundary (Alfè et al. 2002; Labrosse 2003; Jaupart et al. 2015). Using the depth of these phase changes as anchor points, previous studies use isentropic profiles combined with thermal boundary layers to describe a continuous mantle geotherm (e.g., Katsura et al. 2004; Driscoll & Bercovici 2014). Synthesizing these measurements and models has resulted in the following literature estimates for the temperature of the upper mantle (at the base of the lithosphere) and the core-mantle boundary: $T_{UM} = 1587_{-34}^{+161} \text{ K}$ (Jaupart et al. 2015) and $T_{CMB} = 4000 \pm 200 \text{ K}$ (Hirose et al. 2013), respectively.

Over geological time the mantle undergoes solid state convection, transporting heat from the CMB to the surface. The viscosity of the mantle, an important quantity for determining the vigor of mantle convection and heat transfer, is expected to vary significantly between the upper and lower mantle due to variations in temperature, pressure, and composition (Jeanloz & Morris 1986; Boehler 1996; Jaupart et al. 2015). To estimate a 1D (radial) viscosity profile throughout the mantle Paulson et al. (2005) used satellite observations of secular changes in gravity near Hudson Bay to measure Post-Glacial Rebound, or the rate at which land masses gradually bounce back to their hydrostatic level after the melting of massive ice sheets. Implementing 1-D averages of a 3-D viscosity model, Paulson et al. (2005, Fig. 3) constrain the upper mantle (depth $< 1800 \text{ km}$) dynamic viscosity to be $1.5 \times 10^{19} - 1.5 \times 10^{22} \text{ Pa}\cdot\text{s}$, and that of the lower mantle to be $3 \times 10^{19} - 1.5 \times 10^{22} \text{ Pa}\cdot\text{s}$. Assuming an upper and lower mantle density of $\rho_{UM} = 3300 \text{ kg/m}^3$ and $\rho_{LM} = 5200 \text{ kg/m}^3$, respectively, we obtain kinematic viscosity estimates of $\nu_{UM} = 5 \times 10^{15} - 4.5 \times 10^{18} \text{ m}^2/\text{s}$ and $\nu_{LM} = 5 \times 10^{15} - 2.9 \times 10^{18} \text{ m}^2/\text{s}$.

Although surface measurements constrain the upper mantle heat flow to $Q_{UM} = 38 \pm 3 \text{ TW}$ Jaupart et al. (2015), the core-mantle boundary (CMB) heat flow can not be measured directly. However, the temperature jump across the lower mantle thermal boundary layer can be constrained by extrapolating the mantle geotherm down and the inner core boundary (ICB) temperature, i.e. the solidification temperature of the core, up to the CMB. This technique combined with the estimated viscosity of the lower mantle typically gives estimates of $Q_{CMB} = 11 \pm 6 \text{ TW}$ for the CMB heat flow

(Jaupart et al. 2015). Thermal evolution models of the Earth, therefore, must be within these margins of uncertainty to be considered successful.

The subduction of Earth’s tectonic plates drives the upwelling of ambient mantle at mid-ocean ridges, facilitating the cycling of volatiles between the solid interior and atmosphere over geological timescales. The fraction of upwelling mantle that melts and its rate of flow determine the melt mass flux, which also plays a role in heat transport and can have a direct impact on planetary thermal evolution. The extent of melting of mid-ocean ridge basalts (MORB) has been estimated by compiling various measurements of basalt chemistry as a function of axial depth, and averaging the data over large distances to account for small-scale variability in basalt composition (Klein & Langmuir 1987). This analysis suggests that the average extent of MORB melting is 8 – 15% (Gale et al. 2013).

Measurements of crustal production rates at plate boundaries probe mantle melting by providing estimates on the upward mass flux of mantle melt. Cogné & Humler (2004) use direct measurements of currently visible seafloor surfaces bounded by pairs of geophysical isochrones in the Atlantic, Indian, Antarctic, Pacific, Nazca, and Cocos ocean basins to estimate a seafloor production rate of 5 – 15 km³/year. Li et al. (2015) use three-dimensional seismic tomography to measure magmatic accretion at the Southwest Indian Ridge, measuring a crustal production rate of ~20 km³/year, providing an upper bound on mantle melt mass flux. Assuming an upper mantle density of ~3200 kg/m³, a crustal production rate range of 5 – 20 km³/year corresponds to a mantle melt mass flux of $(1.3 \pm 0.8) \times 10^6$ kg/s (values below zero not permitted). The amount of heat transported by the melt has been estimated to be ~1.5 TW (Nakagawa & Tackley 2012).

Earth’s magnetic field is generated by convection in its liquid iron outer core. Core convection is primarily generated compositionally through the solidification of the solid iron inner core, where light elements are rejected into the liquid, thereby decreasing the local density of the fluid and driving fluid flow. The radius of the inner core has been measured to high precision by seismographs, yielding $R_{\text{IC}} = 1224.1 \pm 0.1$ km (Jaupart et al. 2015).

Key measurements of the terrestrial magnetic field include the dipolar magnetic moment, which quantifies the strength of the core field, and magnetopause radius, which is the boundary between the terrestrial magnetic field and that of the solar wind. Measurements of Earth’s magnetic field suggest a terrestrial magnetic moment of 80 ZAm² (de Pater & Lissauer 2010; Kivel-

son & Bagenal 2014), which we define as 1 Earth unit. Similarly, the magnetopause radius is ~9.1 Earth radii (Driscoll & Bercovici 2013), which we also define as 1 Earth unit. While the reported measurements lack formal uncertainty estimates, we adopt conservative validation tolerances of ± 0.015 Earth units for the magnetopause radius and ± 0.05 Earth units for magnetic moment. These $\leq 5\%$ tolerances effectively account for known variability in these quantities: the location of the magnetopause varies with solar wind conditions, while the magnetic dipole moment exhibits secular variation.

1.2. *Models of Processes Driving Earth’s Evolution*

Earth is a complex, coupled system, and key parameters affect each other through interconnected physical and chemical processes. In this section, we summarize recent efforts to model these interdependent processes across Earth’s stellar environment, atmosphere, surface, and interior, including the core, mantle, and lithosphere. We also address some common challenges in modeling Earth’s evolution and discuss proposed resolutions.

1.2.1. *Stellar Modeling*

All stars evolve over time, and our gradually brightening Sun has played an important role in shaping our planet’s climate over 4.5 Gyr. Stellar evolution models are commonly used to quantify changing mass, temperature, and luminosity over time by coupling stellar interior and atmospheric processes. These models have been particularly effective for simulating main sequence stars like our Sun, which grow in radius and luminosity as nuclear fusion slowly exhausts the available hydrogen fuel. Baraffe et al. (2015) used updated molecular line-lists and solar abundances to simulate the evolution of low-mass stars ($M_{\star} \leq 1.4M_{\odot}$), and validate their evolutionary model on color-magnitude observations of stellar populations of various ages. This particular stellar evolution model has been used in a broad number of exoplanet and stellar astronomy applications, including planetary evolution (Luger & Barnes 2015; Do Amaral et al. 2022; Gialluca et al. 2024; Winterhalder et al. 2024).

Stellar evolution models can also be used to simulate the young Sun and thus constrain the stellar environment of the early Earth. Consequently, a broad consensus has emerged that the early Earth orbited a fainter Sun, approximately 70% as bright as it is today (1.0 solar luminosity, L_{\odot} , corresponding to 1370 W/m² incoming solar flux) (Sagan & Mullen 1972; Newman & Rood 1977; Gough 1981). Though the faint young Sun might imply a much colder terrestrial climate, the geological record suggests liquid water persisted on Earth’s

surface as early as the Hadean (4.4 – 4.2 Gya) (Appel et al. 2001; Mojzsis et al. 2001; Wilde et al. 2001; Foriel et al. 2004; Holland 2020) with potentially even warmer surface temperatures than today (Knauth & Epstein 1976; Knauth & Lowe 2003; Tartèse et al. 2016), though intermittent glacial periods may have also occurred (Kasting & Catling 2003). This so-called “faint young Sun” paradox is an issue of ongoing discussion in the astronomy and Earth science communities (Kasting 2010; Goldblatt & Zahnle 2011; Feulner 2012; Charnay et al. 2020; Basinger et al. 2024). Potential resolutions to this paradox primarily focus on the composition of the early Earth’s atmosphere, which we discuss below.

1.2.2. Atmosphere & Climate Modeling

Since planetary evolution models cover Gyr-timescales, previous work has typically simplified the treatment of the atmosphere and climate to maximize computational speed. For example, Driscoll & Bercovici (2013) calculated the radiative contributions of atmospheric CO₂ and H₂O by assuming wavelength-, pressure-, and temperature-independent (i.e., “gray”) molecular opacities for both species. Similarly, these models account for cloud reflectivity by incorporating it into the surface albedo (Driscoll & Bercovici 2013). These gray models inherently do not represent the wavelength-dependent absorption and scattering processes that contribute to planetary energy balance.

A common approach to balancing computational efficiency with physical realism is the use of energy balance models (EBMs), which determine zonal and average surface temperature as a function of latitude by finding the equilibrium point where incoming radiation balances outgoing radiation from the planet (e.g., Budyko 1969; Sellers 1969; North & Coakley Jr 1979; North 2024). In these models, the incoming radiation, or absorbed short-wave radiation (ASR), depends on the incoming stellar flux, planetary orbital distance, and total planetary albedo (including contributions from both the surface and atmosphere). Outgoing long-wave radiation (OLR) is a function of surface temperature and the greenhouse effect of atmospheric constituents. Other approaches use one-dimensional radiative-convective models that explicitly calculate wavelength-dependent radiative transfer, capturing absorption features of greenhouse gases like CO₂, H₂O, and CH₄ (Kasting et al. 1993; Kopparapu et al. 2013). Lastly, three-dimensional general circulation models (3D GCMs) provide full spatial resolution by explicitly simulating atmospheric circulation and thermodynamics, enabling self-consistent treatment of cloud formation, meridional heat transport, and regional climate patterns, though at signifi-

cantly greater computational cost that limits their application to Gyr-timescale planetary evolution studies (e.g., Leconte et al. 2013; Way et al. 2017; Turbet et al. 2018; Fauchez et al. 2019; Charnay et al. 2021; Wolf et al. 2022; Tsigaridis et al. 2025).

Evidence suggests that our atmosphere has supported a warm and wet surface prior to 4.3 Ga (Cameron et al. 2024), motivating modelers to infer early atmospheric composition to resolve the faint young Sun paradox. One hypothesis is that our planet had increased abundances of atmospheric N₂ leading to higher surface pressures and temperatures during the Archean epoch (Goldblatt et al. 2009). However, isotopic analysis of 3.5-billion-year-old hydrothermal quartz suggests that the atmospheric N₂ reservoir has changed little over Earth’s history (Marty et al. 2013), and studies of both fossilized raindrops and the size of gas bubbles in ancient lava flows indicate that the overall surface pressure of the early Earth may have been much *lower* than today (Som et al. 2012, 2016). Another potential explanation is higher abundances of greenhouse gases. Since the atmospheric abundance of H₂O is limited by condensation and therefore surface temperature (Catling et al. 2001), higher abundances of non-condensable greenhouse gases like CO₂ are commonly invoked to explain Earth’s apparent long-term habitability and therefore resolve the faint young Sun paradox (Sagan & Mullen 1972; Kasting 1987; Haqq-Misra et al. 2008). Though other greenhouse gases such as CH₄ have been proposed as additional warming agents for the early Earth (Pavlov et al. 2000), abiotic methane sources generate fluxes several orders of magnitude lower than biological production (Etiope & Sherwood Lollar 2013; Wogan et al. 2020; Thompson et al. 2022). We therefore focus our model on CO₂ and H₂O as the primary greenhouse gases regulating climate on an Earth without life, with a detailed discussion of more reduced species in Section 4.2.

CO₂ is of particular interest due to Earth’s carbonate-silicate cycle, a negative feedback mechanism that is theorized to maintain global thermal equilibrium by redistributing CO₂ between the atmosphere and interior (Walker et al. 1981; Kasting et al. 1993; Berner 2004). However, the effectiveness of this stabilizing mechanism depends critically on the presence of exposed silicate rocks and liquid water at the surface, both of which may vary throughout a planet’s history. Furthermore, the carbonate-silicate cycle couples atmospheric composition to interior dynamics through volcanic outgassing, which is controlled by mantle convection, melt generation, and volcanic eruptions. Understanding how this cycle has operated over Earth’s history, and how it might function on planets with different initial conditions or

evolutionary paths, requires integrating climate models with models of interior processes and volatile cycling.

1.2.3. *Surface and Mantle Modeling*

Plate tectonics facilitates the long-term carbonate-silicate cycle on Earth (Kasting & Catling 2003), and is thus postulated as an essential ingredient of a habitable planet (Foley & Driscoll 2016; Wang et al. 2023). Therefore, Earth's habitability may be attributed to not only its favorable orbital distance, but also its interior producing the geodynamical cycling required to maintain a stable climate. The constant creation of oceanic crust at mid-ocean ridges drives volcanic outgassing of CO₂ from the mantle to the atmosphere, while weathering of exposed silicate rocks removes atmospheric CO₂ and transports it back into the mantle via the subduction of carbonate minerals. This recycling mechanism couples atmospheric composition directly to interior dynamics, with plate speed controlling both the rate of CO₂ injection through volcanism and the rate of CO₂ removal through subduction.

Similarly, the deep water cycle – which exchanges H₂O between the surface ocean and mantle through hydration of subducting oceanic crust and subsequent degassing at mid-ocean ridges and arc volcanoes – plays a crucial role in maintaining habitable surface conditions (Schaefer & Sasselov 2015; Seales & Lenardic 2020). Water content in the mantle affects convective vigor by reducing viscosity, which in turn influences plate speeds, outgassing rates, and the thermal evolution of the planet. The balance between water storage in the mantle versus the surface ocean also affects sea level and continental exposure, further modulating the efficiency of silicate weathering and climate regulation.

Though recent work has proposed that stagnant lid planets may also maintain long-term habitability via crustal delamination (Foley & Smye 2018; Foley 2019), this process likely requires sustained CO₂ outgassing and therefore a highly oxidized mantle hotter than the Earth's (Spohn & Breuer 2016). Furthermore, Foley (2015) showed that plate tectonics promotes higher erosion rates that can prevent a planet from entering a supply-limited weathering regime, which can frustrate climate stabilization. In a supply-limited regime, the rate of weathering is controlled by the availability of fresh rock. Foley (2015) parameterize both continental and seafloor weathering rates to scale with surface temperature, atmospheric $p\text{CO}_2$, and the evolving fractions of exposed land and ocean coverage, allowing their model to capture the transition between kinetically limited and supply-limited weathering regimes. Ultimately, the tectonically active Earth is currently our only ex-

ample of a habitable planet, though the degree to which plate tectonics is necessary versus merely sufficient for habitability remains an open question.

The evolution of plate tectonics over Earth's history is also uncertain, and recent work has argued that Earth may not have always operated in a plate tectonic mode. To explain evidence that the mantle has not cooled at a constant rate over geological time (Herzberg et al. 2010), Condie et al. (2016) invoke a transition from a stagnant lid mode to modern plate tectonics sometime during the Archean epoch. Such a transition would have profound implications for volatile cycling, as the efficiency of CO₂ outgassing and subduction depends critically on the tectonic regime. Alternatively, multistage cooling could also be explained by deep water cycling coupled to mantle convection, where the water content of the mantle affects convective vigor and thus plate speed (Sandu et al. 2011; Crowley et al. 2011; Schaefer & Sasselov 2015; Seales & Lenardic 2020). Water acts to reduce mantle viscosity, enhancing convection and accelerating cooling, while also affecting the depth and extent of mantle melting, which controls the rate of degassing. Seales & Lenardic (2020) showed that a deep water cycle can explain multistage mantle cooling and match observations of mantle temperature evolution within uncertainties, without invoking a transition from a stagnant lid to plate tectonics via serpentinization.

The rates of water regassing and degassing depend on mantle temperature, plate speed, and the solubility of water in the erupting magma, all of which evolve over time. Models that couple water cycling to mantle dynamics typically parameterize the mantle viscosity as a function of mantle water content, capturing the strong feedback where hydrated mantles convect more vigorously, enhancing the rate of water extraction from the mantle (Seales & Lenardic 2020; Garcia et al. 2026). This coupling between water content and mantle dynamics has important implications for surface conditions, as the amount of water stored in the mantle versus the surface ocean affects sea level and continental exposure, and thus the operation of the carbonate-silicate cycle. The evolution of Earth's continental crust is itself an open area of research: though most studies agree that the continental crust has accumulated over time, they differ on the rate at which it was produced and, therefore, how the land fraction has evolved (for a review, see Korenaga 2018). An early Earth with a higher ocean surface fraction would potentially have a lower planetary albedo and thus absorb more solar radiation, offsetting the cooling effect of a fainter Sun (Schatten & Endal 1982; Cogley & Henderson-Sellers 1984; Gérard et al. 1992; Jenkins 1993; Molnar & Gutowski Jr 1995;

Rosing et al. 2010; Feulner 2012). However, some models suggest that higher surface ocean fraction can actually lead to a higher albedo due to enhanced evaporation and cloud formation (Jenkins 1995a,b, 1999; Feulner 2012).

Another factor affecting mantle evolution and volatile outgassing is the solidification of the early magma ocean and possible presence of a basal magma ocean (BMO), a layer of molten or partially molten material at the base of the mantle above the core-mantle boundary. If the early Earth’s magma ocean gradually solidified downward toward the core, it would have partitioned radiogenic elements that are incompatible with solid mantle minerals into the liquid, enriching the residual BMO in heat-producing isotopes like ^{40}K , ^{232}Th , ^{235}U , and ^{238}U (Boyett & Carlson 2005; Labrosse et al. 2007). With potential enrichment as high as \sim 500 times the solid mantle (Labrosse et al. 2007), the BMO may provide a stable, thermally insulating layer that slows core cooling. While a BMO likely does not exist in Earth’s present-day lower mantle, the thermal boundary layer at the base of the mantle may play a similar role, insulating the core and increasing the longevity of the dynamo (Labrosse et al. 2007). However, the existence of the BMO is not yet widely accepted (Jackson et al. 2010; Campbell & O’Neill 2012; Carlson et al. 2014). For example, Campbell & O’Neill (2012) note that the measured heat flux from upper mantle plumes is inconsistent with a radioactively-enriched layer in the lower mantle.

Lastly, the solidification of the magma ocean following accretion, though brief (1–100 Myr), likely dictated the initial composition of the atmosphere (Elkins-Tanton 2008; Lammer et al. 2018; Stueeken et al. 2020; Chao et al. 2021; Carone et al. 2025). However, given the uncertainties in early Earth conditions and the complexity of this problem, we do not explicitly model magma ocean solidification in this work. Instead, we choose a set of initial conditions that apply after the bulk of the mantle has solidified.

1.2.4. Core Modeling

Earth’s long-lived magnetic field has been maintained by convection in the liquid iron-rich outer core (Busse 1976; Olson & Christensen 2006; Driscoll & Wilson 2018). Core convection today is driven by a combination of thermal and compositional buoyancy. Thermal convection occurs when the CMB heat flow exceeds the conductive heat flow limit, which is set by the core’s intrinsic adiabatic gradient and thermal conductivity. Recent measurements of the thermal conductivity of iron-rich alloys at core-conditions vary significantly, from 40–200 W/m/K (Ohta et al. 2016; Konôpková et al. 2016), although more moderate values have been recently argued

(Pozzo et al. 2022). The majority of the heat drawn out of the core is likely secular heat from formation. Although radiogenic elements in the core may also contribute to internal heating, partitioning experiments favor very low abundances (Chidester et al. 2022). Of these elements, uranium is the most abundance radiogenic element in the core (Chidester et al. 2022), with an approximate production rate of \sim 0.8 TW.

Another important contribution to convection in the core is compositional buoyancy driven by inner core solidification. Compositional buoyancy is produced when light elements are expelled from the solidifying inner core, enriching the surrounding fluid and lowering its density. Presently it is thought that the continuous solidification of the solid inner core provides the majority of the energy required to drive convection and generate Earth’s geomagnetic field. However, paleomagnetic evidence suggests that Earth’s magnetic field predates the initial nucleation of the inner core, perhaps by billions of years, implying a different buoyancy source must have maintained the earlier geomagnetic field. One solution to this “new core paradox” is to invoke higher core radioactivity (>2.5 TW), though this seems unlikely given the low partitioning of radiogenic elements into iron versus silicate liquids (Blanchard et al. 2017; Bouhifd et al. 2007; Chidester et al. 2017, 2022; Corgne et al. 2007; Hirao et al. 2006; Watanabe et al. 2014; Xiong et al. 2018; Driscoll & Davies 2023). Alternatively, a former BMO may have become enriched in radiogenic elements that were expelled from the solidifying mantle above it (Boyett & Carlson 2005; Labrosse et al. 2007; Jackson et al. 2010; Lee et al. 2010; Tolstikhin & Hofmann 2005; Driscoll & Davies 2023; Boukaré et al. 2025), but this scenario remains widely debated (Campbell & O’Neill 2012; Carlson et al. 2014; Jackson et al. 2010).

1.3. Previous Whole-Planet Modeling

The emerging concept of “whole-planet” modeling was first introduced in a pair of papers (Driscoll & Bercovici 2013; Foley & Driscoll 2016), where it is argued that long-term habitability depends on evolving interior-atmosphere volatile exchange. Foley & Driscoll (2016) argue that climate influences whether or not plate tectonics develops, as low surface temperatures promote long-lived weak shear zones, or “damage”, in the lithosphere. In turn, plate tectonics facilitates volatile recycling at plate boundaries, which is particularly important for stabilizing the climate via the carbon cycle. Climate, therefore, can also affect the cooling rate of the interior, ultimately influencing the core cooling rate and thus magnetic field generation. Finally, the strength of the planetary magnetic field affects the rate of at-

mospheric escape, hypothesized to be a major factor in the desiccation of Venus and thus its distinct evolutionary path (Watson et al. 1981; Driscoll & Bercovici 2013; Gillmann et al. 2022).

Despite its potential importance, many questions about whole planet modeling remain. Krissansen-Totton et al. (2021) developed a rigorously coupled mantle-surface-atmosphere model, which includes a magma ocean phase and a transition from a mobile lid to plate tectonics, to explore the long-term carbon and oxygen cycles. However, they did not focus on the coupled evolution of the mantle and core, instead assuming that the core cooling decays exponentially. Drawing on the ideas of Nimmo (2002), Armann & Tackley (2012) argue that the surface and core are interconnected, demonstrating that an episodic stagnant lid can suppress core cooling. Building on this work, Garcia et al. (2026) produced a coupled one-dimensional solar-atmosphere-lithosphere-mantle-core model of Venus that reproduces present-day atmospheric H₂O and CO₂ abundances and the lack of a core dynamo. Their ability to validate the model is limited by the dearth of observations of Venus's surface and interior. Furthermore, as in Driscoll & Bercovici (2013), Garcia et al. (2026) assume a gray atmospheric model. To calculate the planet's energy balance, Krissansen-Totton et al. (2021) use a pre-calculated radiative transfer grid to solve for the wavelength-dependent OLR from the planet, and use a simple parameterization of albedo, planet-star distance, and stellar luminosity to solve for the ASR. Thus, no whole-planet evolutionary model yet includes radiative transfer calculations to solve for the ASR and OLR balance of the changing planetary climate.

The presence of these interconnected feedback mechanisms make clear that long-term planetary evolution cannot be fully understood by studying individual subsystems in isolation. The stellar environment, atmosphere, surface, mantle, and core form a coupled system where changes in one component may cascade to the whole system over geological timescales. For example, the evolution of atmospheric composition – the primary observable for missions like HWO – is mediated not only by photochemistry and climate, but also by outgassing set by mantle convection and water content, which in turn depend on the thermal state of the core and mantle. To correctly interpret observations of Earth-like exoplanets and establish a robust null hypothesis for biosignature detection, we require validated whole-planet models that self-consistently track the co-evolution of all major planetary reservoirs. The pre-industrial Earth, with its relatively well-constrained

properties across all subsystems, provides one possible validation target for such models.

2. METHODS

Our fully-coupled model builds on **vPLanet** (Barnes et al. 2020; Garcia et al. 2026) by incorporating published models of the carbon cycle (Foley 2015), the deep water cycle (Seales & Lenardic 2020), the surface hydrological cycle (Driscoll & Bercovici 2013), and climate (Wogan et al. 2025b) for planets with plate tectonics. Our abiotic Earth model components are summarized in the schematic in Figure 1, with a more detailed schematic of CO₂ and H₂O cycling between the interior, surface, and atmosphere shown in Figure 2.

In this section we describe the governing equations used to upgrade **vPLanet**'s **ThermInt** module. Any equations and physical parameters not detailed here are implemented as described by Barnes et al. (2020, Appendix K). Model constants are defined in Appendix A.

2.1. Core, Mantle, and Basal Magma Ocean

We use the **vPLanet** core-mantle interior module, **ThermInt**, and the radiogenic heating module, **RadHeat**, as described by Barnes et al. (2020). We make two key modifications to the nominal model: (1) a basal magma ocean (BMO) layer, which treats radiogenic heating contributions from both the core and the BMO in one combined term prior to present-day solidification, and (2) a mantle viscosity influenced by the water content in the mantle as described in Garcia et al. (2026). The mantle water content is controlled by the deep water cycle and is described in Section 2.3.

Earth's mantle may have solidified from the middle out (Boukaré et al. 2025), where a prolonged basal magma ocean (BMO) would have solidified slowly and become enriched in incompatible elements, including radiogenic species of K, Th, and U (Labrosse et al. 2007). To capture the thermal affect of an enriched BMO we define a new effective BMO + core radiogenic heating rate, $Q_{\text{rad},\text{BMO}+C} = Q_{\text{rad},\text{BMO}} + Q_{\text{rad},C}$ that folds in the radiogenic heating of the BMO. With this modification the core energy balance in **ThermInt** becomes:

$$\dot{T}_C = \frac{Q_{\text{BMO}} - Q_{\text{rad},\text{BMO}+C}}{M_C c_C + \frac{dM_{IC}}{dT_C} (L_H + E_G)}, \quad (1)$$

where M denotes mass, c_C denotes the core specific heat capacity, \dot{T} denotes the evolving reservoir temperature, and Q denotes heat flow. The subscripts indicate the relevant reservoir, where C , CMB, and BMO represent the core, core-mantle-boundary, and basal magma ocean layer, respectively. Thus, $Q_{\text{rad},\text{BMO}}$ represents the radiogenic heat production in the BMO, and $Q_{\text{rad},C}$ rep-

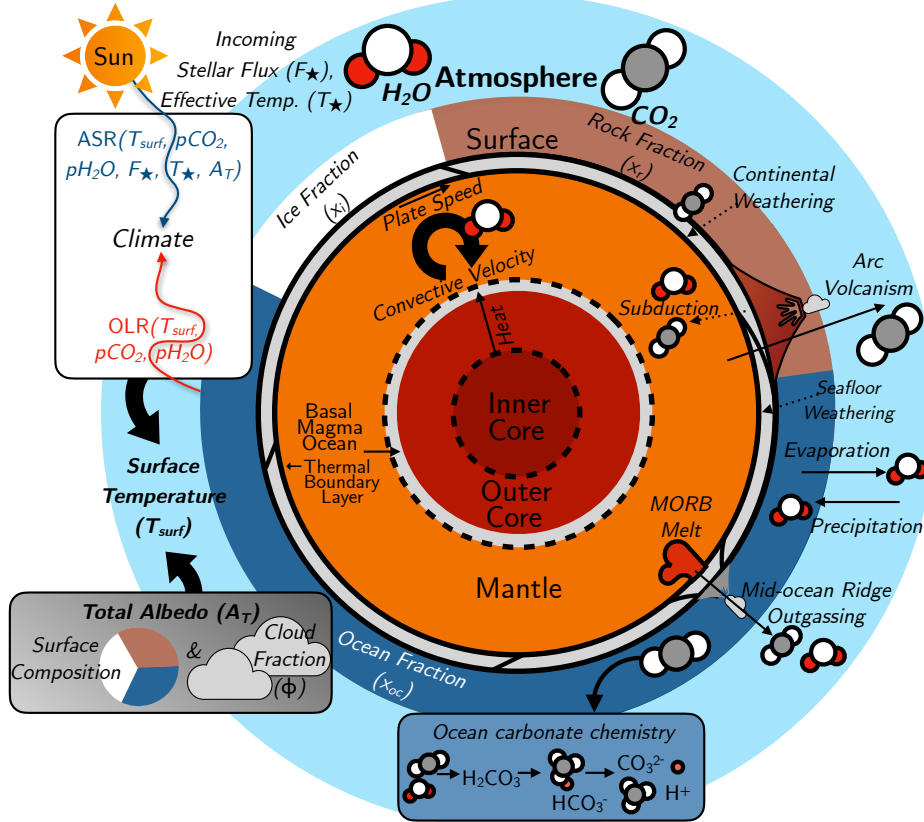


Figure 1. A schematic of the key processes included in our abiotic Earth model. Remotely observable quantities (surface temperature, albedo, and atmospheric H_2O and CO_2) are in bold. Volatile cycling is diagrammed in more detail in Figure 2.

resents the radiogenic heat production in the core. Additionally, $\frac{dM_{IC}}{dT_C}$ is the derivative of the inner core mass with respect to core temperature, and L_H and E_G give the latent and gravitational energy released at the inner core boundary per unit mass. For the full derivation, see Appendix B.

This approach approximates the effect of a BMO enriched in radiogenic elements without modeling its solidification. In reality, as the mantle gradually solidifies downward towards the core and the liquid BMO shrinks, it becomes further enriched in radiogenic elements (Labrosse et al. 2007). This effectively maintains a higher concentration of radiogenic elements outside the core and provides a stable thermally insulating layer.

To match estimates of upper mantle heat flow within $1-\sigma$ uncertainty, we find that our model requires approximately 3.5 TW of combined core and lower mantle power by 4.5 Gyr. However, core radiogenic heating today may be as low as zero. To assess whether this excess heating is physically plausible, we calculate the mass of ^{40}K in the BMO required to generate ~ 3.5 TW.

Labrosse et al. (2007) estimate that if the early Earth's magma ocean gradually solidified downward toward the core, incompatible radiogenic elements would be ex-

pelled from solid mantle minerals and concentrated in the remaining liquid BMO. They find the primordial BMO could be enriched in the main radioactive elements (^{40}K , ^{232}Th , ^{235}U , and ^{238}U) by as much as 500 times the concentrations in the solid mantle (see their Figure 4). Owing to its short half-life, ^{40}K makes the largest contributions to radiogenic power by the end of the evolution – 10 times that of ^{232}Th , 100 times that of ^{238}U , and 1000 times that of ^{235}U . Therefore, we assume the contributions from U and Th in the BMO are negligible, and only consider the decay of ^{40}K in the BMO.

We can compute the mantle and BMO concentrations of ^{40}K after 4.5 Gyr to determine the radioactive enrichment required to explain the excess core heating. We assume that the primordial BMO is a spherical shell with thickness 20 km, which is in agreement with estimates of the size of ultra-low velocity zones at the core-mantle boundary (Hansen et al. 2020). We also assume that the BMO is characterized by a slightly higher density than the solid mantle due to its relative enrichment in iron (6000 kg m^{-3}). We calculate a concentration ratio of $3.37 \times 10^{-7} / 1.46 \times 10^{-8} = 23.0$ between the BMO and the solid mantle (see Appendix B for the full calculation). Thus, to explain excess heating of 3.5 TW, we

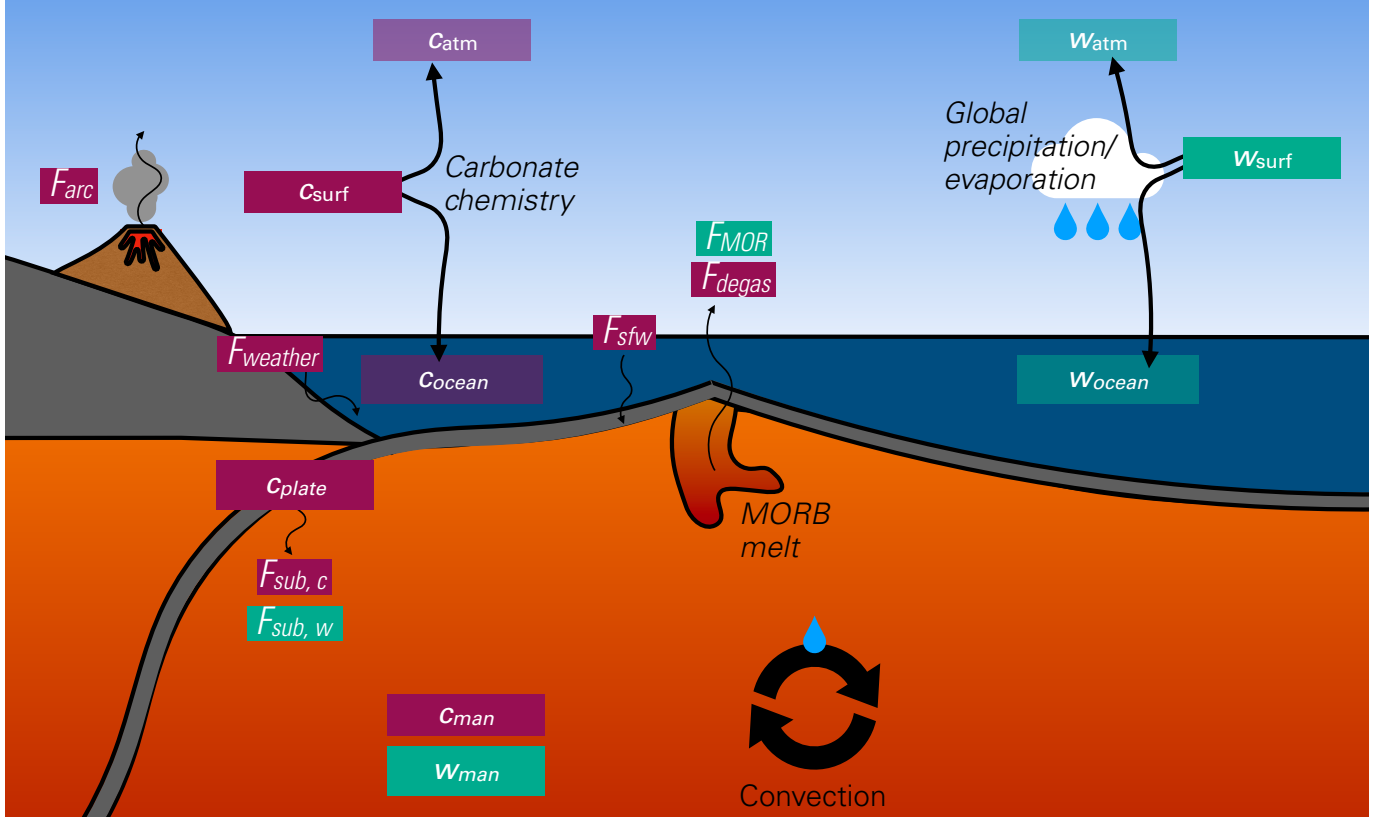


Figure 2. A schematic showing the atmospheric sources and sinks that define the new volatile cycling processes in vPLanet’s ThermInt module, inspired by Figure 1 in Foley (2015). Fluxes related to CO_2 are color-coded magenta, and fluxes related to H_2O are color-coded teal. We incorporate the climate-stabilizing carbon cycle from Foley (2015), tracking the mass of CO_2 across the mantle (c_{man}), plate (c_{plate}), and surface (c_{surf}) reservoirs. We include the deep water cycle from Seales & Lenardic (2020), and a precipitation/evaporation parameterization from Driscoll & Bercovici (2013), which allow us to track the mass of H_2O across the mantle (w_{man}) and surface (w_{surf}) reservoirs. At each timestep, surface carbon and water are partitioned into the atmosphere ($c_{\text{atm}}, w_{\text{atm}}$) and the ocean ($c_{\text{ocean}}, w_{\text{ocean}}$) by enforcing equilibrium at the air-water boundary. This schematic does not depict modeled ocean chemistry.

require a BMO with ^{40}K concentration only ~ 23 times larger than that of the solid mantle – well within the factor of 500 enrichment estimated by Labrosse et al. (2007). This margin allows for considerable uncertainty in our assumptions. For example, if the BMO is only 1 km thick, the required ^{40}K enrichment would still be ≤ 500 times the solid mantle concentration, remaining consistent with theoretical predictions.

2.2. Carbon Cycle

The model conserves the mass of CO_2 over geological time as it cycles between three reservoirs: the mantle (c_{man}), plate (c_{plate}), and surface (c_{surf}), which includes the ocean (c_{ocean}), and atmosphere (c_{atm}) reservoirs. At each time step, we calculate the following fluxes as in Foley (2015): arc volcanic (F_{arc}), continental weathering (F_{weather}), seafloor weathering (F_{sfw}), degassing (F_{degas}), and subduction ($F_{\text{sub},c}$) (see Figure 2). The fluxes are balanced between the planet’s CO_2 reservoirs according to the following equations (Foley 2015):

$$\dot{c}_{\text{plate}} = \frac{F_{\text{weather}}}{2} + F_{\text{sfw}} - F_{\text{sub},c}, \quad (2)$$

$$\dot{c}_{\text{man}} = (1 - f)F_{\text{sub},c} - F_{\text{degas}}, \quad (3)$$

where f is a constant that defines the fraction of subducted CO_2 that degasses. The continental weathering flux is divided by a factor of 2 to account for the fact that half of the carbon initially sunk into the continental plate is returned to the atmosphere when carbonates form on the seafloor (Berner et al. 1983; Foley 2015). Finally, we have

$$\dot{c}_{\text{surf}} = F_{\text{arc}} + F_{\text{degas}} - \frac{F_{\text{weather}}}{2} - F_{\text{sfw}}, \quad (4)$$

where by mass conservation $c_{\text{surf}} = c_{\text{atm}} + c_{\text{ocean}}$ (see Section 2.5 for a detailed description of partitioning CO_2 into the atmosphere and ocean).

We define the fluxes according to Foley (2015), with some minor changes. The subduction flux is given by

$$F_{\text{sub}} = 2c_{\text{plate}}vL \times \frac{d_{\text{melt}}}{V_{\text{man}}}, \quad (5)$$

where v is the speed of the tectonic plates (see below), L is the present-day length from the ocean ridge to the trench, d_{melt} is the depth to the base of the upper mantle melt region (see Barnes et al. (2020, Appendix K)), and V_{man} is the volume of the mantle. The $d_{\text{melt}}/V_{\text{man}}$ term represents division by the effective area of the mantle melt. The arc volcanic flux is subsequently defined as

$$F_{\text{arc}} = fF_{\text{sub}}, \quad (6)$$

where f is the fraction of subducted carbon that degasses. The degassing flux is given by

$$F_{\text{degas}} = 2f_{\text{UM}}f_d c_{\text{man}} \frac{vLd_{\text{melt}}}{V_{\text{man}}}, \quad (7)$$

where f_{UM} is the upper mantle melt fraction, f_d is the fraction of the upwelling mantle that degasses, and V_{man} is the volume of the mantle. We include the additional f_{UM} term to ensure that the degassing flux is tightly coupled to the size of the melt layer. We note that the upper mantle melt fraction describes partial melting of the upwelling mantle, and not the whole-mantle volumetric melt fraction typically used in models which parameterize the solidification of the magma ocean (e.g., Elkins-Tanton 2008; Krissansen-Totton et al. 2021).

The arc and ridge degassing fluxes are the CO₂ sources in the surface (atmosphere + ocean). Both terms include efficiency factors f and f_d . We calibrate these factors to give a total carbon outgassing flux similar to present-day observations of $\sim 1\text{--}5$ Tmol/yr (Kerrick 2001), as well as PIE pCO₂ values.

Prior to subduction, seafloor and continental weathering deposit carbon into the oceanic plate. Foley (2015) gives the seafloor weathering flux as

$$F_{\text{sfw}} = F_{\text{sfw},0} \left(\frac{v}{v_0} \right) \left(\frac{x_{\text{oc}}}{x_{\text{oc},0}} \right) \left(\frac{p\text{CO}_2}{p\text{CO}_{2,0}} \right)^{\alpha_1}, \quad (8)$$

where $F_{\text{sfw},0}$ is the present-day seafloor weathering flux, v_0 is the present-day speed of the tectonic plates, x_{oc} gives the ocean surface fraction, and $x_{\text{oc},0}$ represents the present-day ocean surface fraction of 0.71. Lastly, $p\text{CO}_2$ is the partial pressure of CO₂, $p\text{CO}_{2,0}$ is its present-day value, and α_1 quantifies the dependence of basalt carbonation on atmospheric CO₂.

Finally, Foley (2015) derives a continental weathering flux that accounts for supply-limited behavior at high pCO₂ such that

$$F_{\text{weather}} = F_{\text{weather},s} \times \left\{ 1 - \exp \left[-\frac{F_{\text{weather},0}}{F_{\text{weather},s}} x_r \left(\frac{v}{v_0} \right)^{\alpha_2} \right. \right. \\ \times \left(\frac{p\text{CO}_2}{p\text{CO}_{2,0}} \right)^{\beta_1} \left(\frac{P_{\text{sat}}}{P_{\text{sat},0}} \right)^{a_1} \\ \left. \left. \times \exp \left(\frac{E_a}{R_g} \left(\frac{1}{T_{\text{surf},0}} - \frac{1}{T_{\text{surf}}} \right) \right) \right] \right\}, \quad (9)$$

where $F_{\text{weather},s}$ is the supply limit to weathering, $F_{\text{weather},0}$ is the present-day silicate weathering rate, β_1 is the partial pressure of CO₂ (pCO₂) scaling parameter for silicate weathering, P_{sat} is the saturation vapor pressure, $P_{\text{sat},0}$ is the present-day saturation vapor pressure, a_1 is the saturation vapor pressure scaling parameter for silicate weathering, E_a is the activation energy of the weathering reaction, R_g is the universal gas constant, T_{surf} is the surface temperature (see Section 2.7), and $T_{\text{surf},0}$ is the present-day surface temperature. The equation also includes a term for scaling the evolving exposed rock fraction, x_r , at a given time step by the present-day land fraction, $x_{l,0}$. Similar to the seafloor weathering flux equation, we incorporate a scaling factor related to the present-day plate speed raised to the power of α_2 to account for the strength of the dependence of weathering on plate speed. The treatment of evolving surface composition is described in further detail in Section 2.6. The seafloor and continental weathering fluxes strongly influence the pCO₂ evolution in our model. Though there is not an explicit dependence on surface temperature in the seafloor weathering parameterization, it is implicitly dependent on surface temperature via the pCO₂ and plate speed terms.

The supply limit to weathering represents the maximum achievable flux given the available weatherable rock on the surface of the planet. We calculate the supply limit using the relation $F_{\text{weather},s} = (A_{\text{Earth}}x_r E_{\text{max}}f_{cc}\rho_r)/\bar{m}_{cc}$, where E_{max} is the maximum erosion rate, f_{cc} is the fraction of Mg, Ca, K, and Na in the continental crust, ρ_r is the density of the regolith, and \bar{m}_{cc} is the average molar mass of Mg, Ca, K, and Na (Foley 2015). This relation gives the supply-limit in units of mol/s, which we convert to kg/s by multiplying by the molar mass of CO₂, \bar{m}_c . The saturation vapor pressure is related to its present-day value and the surface temperature of the planet according to the relation

$$P_{\text{sat}} = P_{\text{sat,ref}} \exp \left[-\frac{\bar{m}_w L_w}{R_g} \left(\frac{1}{T_{\text{surf}}} - \frac{1}{T_{\text{sat,ref}}} \right) \right], \quad (10)$$

where \bar{m}_w is the molar mass of water, L_w is the latent heat of water, and $T_{\text{sat,ref}}$ is the reference saturation vapor temperature (Driscoll & Bercovici 2013).

The fluxes F_{arc} , F_{sfw} , F_{degas} , and $F_{\text{sub,c}}$ are related to the speed of the tectonic plates, v . We implement the [Seales & Lenardic \(2020\)](#) parameterization, which relates v to the mantle Rayleigh number:

$$v = \frac{a_2 \kappa}{2(R_{\text{man}} - R_c)} \left(\frac{Ra}{Ra_{\text{crit}}} \right)^{2\beta_2}, \quad (11)$$

where a_2 and β_2 are scaling terms, κ is the thermal diffusivity, R_{man} is the radius of the mantle, R_c is the radius of the core, Ra is the mantle Rayleigh number (see [Barnes et al. \(2020\)](#), Appendix K), and $Ra_{\text{crit}} = 660$ is the critical Rayleigh number.

2.3. Water Cycle

We track the mass of water as it cycles between the mantle (w_{man}) and the surface (w_{surf}), which includes the ocean (w_{ocean}), and the atmosphere (w_{atm}), via a subduction flux ($F_{\text{sub,w}}$) and a mid-ocean ridge degassing flux (F_{MOR}). The fluxes balance according to the following system of differential equations:

$$\dot{w}_{\text{man}} = F_{\text{sub,w}} - F_{\text{MOR}} \quad (12)$$

and

$$\dot{w}_{\text{surf}} = F_{\text{MOR}} - F_{\text{sub,w}}, \quad (13)$$

where mass conservation requires that $w_{\text{surf}} = w_{\text{ocean}} + w_{\text{atm}}$.

The abundance of water in the mantle impacts the viscosity of the upper mantle and thus the efficiency of heat transfer via the Arrhenius viscosity. [Garcia et al. \(2026\)](#) give the Arrhenius component of the viscosity as

$$\nu_{\text{Arr}} = \nu_{\text{ref}} \times \exp \left[\frac{E_{a,\text{man}}}{T_{\text{UM}} R_g} - \frac{\Delta E_{\text{H}_2\text{O}}(w_{\text{man}}/M_{\text{man}})}{T_{\text{UM}} R_g} \right], \quad (14)$$

where ν_{ref} is the reference viscosity of the upper mantle, $E_{a,\text{man}}$ is the viscosity activation energy of the upper mantle, $\Delta E_{\text{H}_2\text{O}}$ is the depression of mantle viscosity activation energy due to water, M_{man} is the mass of the mantle, and T_{UM} is the temperature of the upper mantle. The viscosity of the upper mantle is then calculated by dividing the Arrhenius viscosity term by the upper mantle viscosity melt factor ([Garcia et al. 2026](#)). The melt viscosity factor is calculated following [Driscoll & Barnes \(2015\)](#). First, we define the normalized melt fraction:

$$\Phi = \frac{f_{\text{UM}}}{\phi_s}, \quad (15)$$

where f_{UM} is the upper mantle melt fraction and $\phi_s = 0.8$ is the reference melt fraction parameter. Next, we calculate the melt geometry factor:

$$F = (1 - \xi) \cdot \text{erf} \left[\frac{\sqrt{\pi}}{2(1 - \xi)} \Phi (1 + \Phi^\gamma) \right], \quad (16)$$

where the viscosity-melt reduction coefficient $\xi = 5 \times 10^{-4}$, the viscosity-melt reduction exponent $\gamma = 6.0$, and erf is the error function. Finally, the melt viscosity reduction factor is given by:

$$\eta_{\text{melt}} = \frac{1 + \Phi^\delta}{(1 - F)^{B\phi_s}}, \quad (17)$$

where the viscosity-melt reduction exponent $\delta = 6.0$ and the viscosity-melt reduction parameter $B = 2.5$ ([Bercovici et al. 2015](#)).

To calculate the fluxes of water into and out of the mantle, we assume the definitions of $F_{\text{sub,w}}$ and F_{MOR} given by [Seales & Lenardic \(2020\)](#) so that

$$F_{\text{sub,w}} = f_h \rho_{\text{man}} D_{\text{hydr}} S \chi_r, \quad (18)$$

where f_h is the mass fraction of water in the serpentinized layer, ρ_{man} is the density of the mantle, D_{hydr} is the thickness of the serpentinized layer, S is the spreading rate of the tectonic plates, and χ_r is the regassing efficiency factor. The thickness of the serpentinized layer is related to surface temperature T_{surf} according to the relation $D_{\text{hydr}} = (k |T_{\text{surf}} - 973|)/q_m$, where k is the thermal conductivity and q_m is the heat flux through the upper mantle (see [Barnes et al. \(2020\)](#), Appendix K). Note that this parameterization of the subduction flux assumes that there is always a sufficient supply of water to drive the serpentinizing reaction. The spreading rate is related to the speed of the plates as $2Lv$, where the factor of $2L$ represents lateral spreading in both directions. The mid-ocean ridge degassing flux is thus given by

$$F_{\text{MOR}} = \rho_{\text{man}} f_{\text{UM}} X_{\text{melt}} D_{\text{melt}} S \chi_d, \quad (19)$$

where X_{melt} is the abundance of water in the erupting magma, D_{melt} is the depth of the melt zone, and χ_d is the degassing efficiency factor. The parameters f_{UM} and D_{melt} are calculated as described by [Barnes et al. \(2020\)](#), Appendix K), while the fraction of water in the melt can be found by taking $X_{\text{melt}} = \chi_m/[D_{\text{H}_2\text{O}} + f_{\text{UM}}(1 - D_{\text{H}_2\text{O}})]$, where χ_m is the mass fraction of water in the mantle ($w_{\text{man}} / M_{\text{man}}$) and $D_{\text{H}_2\text{O}}$ is the bulk distribution coefficient ([Seales & Lenardic 2020](#)).

The mass of H_2O on the surface (atmosphere + ocean) results from the balance of the mid-ocean ridge degassing sources and the subduction sinks at the plate boundaries. In our model, both terms include degassing and regassing efficiency factors, χ_d and χ_r , respectively.

We tune these factors to give the PIE mass of water in the oceans and atmosphere after 4.5 Gyr, and to give a degassing flux on the order of present-day observations, ~ 11 Tmol/yr (Fischer 2008).

2.4. Atmospheric Constituents

Our Earth-like atmospheres consist of N_2 , H_2O , and CO_2 . As in previous work (Krissansen-Totton et al. 2021), we assume that the atmosphere maintains a constant 1 bar of N_2 , since our 1-bar, abiotic atmospheres lack photosynthetic oxygen. Atmospheric H_2O and CO_2 are allowed to vary based on the balance of sources and sinks from volatile cycling. We do not include atmospheric escape in our model given we aim only to validate the model on the PIE, when escape rates were likely insignificant.

We neglect CH_4 in our model, as abiotic methane fluxes are insufficient to contribute meaningfully to Earth's greenhouse warming. Modern terrestrial observations show that abiotic CH_4 sources – including volcanic outgassing, serpentinization, and hydrothermal processes – generate approximately 1.6 Tg/yr (0.1 Tmol/yr) (Etiope & Sherwood Lollar 2013), while biological sources produce 500–600 Tg/yr (31–37 Tmol/yr) (Saunois et al. 2019), a factor of approximately 300 times larger. Laboratory experiments and thermodynamic modeling support these observational constraints: McCollom (2003, 2016) found that kinetic barriers limit abiotic methane production rates even under thermodynamically favorable conditions, and Wogan et al. (2020) demonstrated that volcanic CH_4 fluxes remain orders of magnitude below biological rates even under highly reducing mantle conditions.

Even on the early, more volcanically active Earth, abiotic methane production would have been substantially lower than microbial methanogenesis. Modern atmospheric methane reaches approximately 1.7 ppmv (Dlugokencky et al. 2011), requiring biological fluxes of 500–600 Tg CH_4 yr $^{-1}$ to persist against photochemical destruction. With abiotic production rates 300 times lower, steady-state methane mixing ratios would remain negligible even with extended atmospheric lifetimes in an anoxic atmosphere (Pavlov et al. 2001), and are thus unlikely to contribute significantly to greenhouse warming compared to CO_2 and H_2O .

In the model framework, we treat both H_2O and CO_2 as combined surface reservoirs. At each time step, we partition each gas between the atmosphere and the ocean by enforcing instantaneous equilibrium. Thus, by mass conservation we require that $c_{\text{surf}} = c_{\text{ocean}} + c_{\text{atm}}$, and $w_{\text{surf}} = w_{\text{ocean}} + w_{\text{atm}}$. Here, we describe the par-

titioning of water, while the partitioning of CO_2 is described in the following subsection.

To maintain hydrostatic equilibrium at the air-water boundary, at each time step we partition water between the atmosphere and the ocean by initially calculating the mass of water in the atmosphere (w_{atm}) in excess of the amount of moisture the air can hold at a given time step (Driscoll & Bercovici 2013). Since the Earth's oceans and atmosphere achieve equilibrium on the order of days, whereas `ThermInt` processes evolve on geological timescales, we assume the flow of water between the atmosphere and the ocean occurs instantaneously in the model. At each time step, we calculate the saturation vapor pressure (Foley 2015) as a function of T_{surf} , and we then multiply by a factor of $RH \times (M_{\text{atm}, \text{T}}/P_{\text{T}}) \times (\bar{m}_w/w_{\text{atm}})$ to obtain m_{moist} , the maximum mass of water that the air can hold, where RH represents the tuneable global average relative humidity.

When $w_{\text{atm}} > m_{\text{moist}}$, the excess water mass is subtracted from w_{atm} and added to w_{ocean} . In the inverse case when $w_{\text{atm}} < m_{\text{moist}}$, to maintain equilibrium between the air and the ocean, we subtract the mass difference from w_{ocean} and add it to w_{atm} . To obtain $p_{\text{H}_2\text{O}}$ in Pa, we convert w_{atm} to moles of H_2O , divide by the total moles in the atmosphere, and multiply by P_{T} . This simplified 0-D approximation provides the initial atmospheric H_2O partial pressure needed as input to the climate calculation (Section 2.7), where it is subsequently refined using the vertically-resolved atmospheric structure.

2.5. Ocean Chemistry

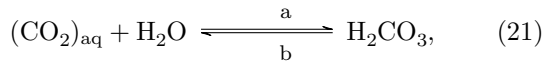
The total reservoir of carbon in the ocean (total dissolved inorganic carbon, or DIC) is the sum of the aqueous $[\text{CO}_2]$, $[\text{CO}_3^{2-}]$, and $[\text{HCO}_3^-]$. Since we enforce equilibrium at the air-ocean boundary, we assume that all ocean chemistry values are representative of surface waters. Initially, atmospheric CO_2 dissolves into ocean water following Henry's law (Pilson 2012), which quantifies the solubility of a gas according to its partial pressure above a liquid so that,

$$(\text{CO}_2)_{\text{aq}} = H \times p\text{CO}_2, \quad (20)$$

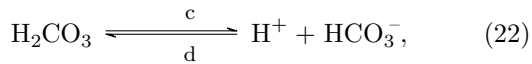
where $(\text{CO}_2)_{\text{aq}}$ gives the aqueous concentration of CO_2 in units of mol/kg H_2O , H is Henry's law coefficient in units of mol/kg/atm, and $p\text{CO}_2$ is the partial pressure of atmospheric CO_2 . We obtain c_{ocean} by multiplying $(\text{CO}_2)_{\text{aq}}$ by the total mass of water in the ocean, w_{ocean} , and the molar mass of CO_2 . By definition, $c_{\text{atm}} = (p\text{CO}_2/P_{\text{T}}) \times (\bar{m}_c/\bar{m}_{\text{atm}}) \times M_{\text{atm}, \text{T}}$, where P_{T} is the total pressure, \bar{m}_{atm} is the average molar mass of the

atmosphere, and $M_{\text{atm}, T}$ is the total mass of the atmosphere. Substituting $p\text{CO}_2 = \text{CO}_{2\text{aq}}/H$ into the mass conservation constraint, we solve a quadratic equation to obtain $(\text{CO}_2)_{\text{aq}}$ based on the integration of Equation (4) at each time step. Finally, to obtain $p\text{CO}_2$ in Pa, we take the $(\text{CO}_2)_{\text{aq}}$ solution and divide by the Henry's law coefficient, and convert from atm to Pa.

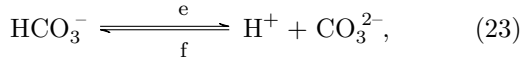
Next, aqueous CO_2 and H_2O combine to make carbonic acid in the following equilibrium reaction:



where the forward reaction (a) is governed by the rate constant k_a , and the reverse reaction (b) is governed by the rate constant k_b . Depending on the ocean pH, carbonic acid readily dissolves into H^+ and bicarbonate in the following equilibrium reaction



with k_c and k_d for the forward and reverse reactions, respectively. Finally, bicarbonate may further dissolve into H^+ and a carbonate ion



where k_e and k_f give the dissolution and combination rate constants, respectively.

As in Schwieterman et al. (2019b) and Krissansen-Totton et al. (2021), we assume that calcite is saturated so that

$$[\text{CO}_3^{2-}] = \frac{\Omega_{\text{cal}} \times K_{\text{sp}}(T_{\text{surf}})}{[\text{Ca}^{2+}]}, \quad (24)$$

where Ω_{cal} is the unit-less global ocean calcite saturation factor, K_{sp} is the calcite solubility product, and $[\text{Ca}^{2+}]$ is the concentration of calcite in the oceans in mol/kg. To calculate solubility self-consistently with surface temperature, we use the temperature and salinity-dependent solubility product formula given by Millero (2005). As in Schwieterman et al. (2019a), for all solubility parameterizations we assume that ocean salinity remains constant at 35 parts per thousand. We also assume that the temperature of the ocean is equivalent to the global average surface temperature, as we assume that the ocean and atmosphere equilibrate faster than our model's geological timescales.

Using Equation (24), a saturation factor, and a calcite concentration, we can calculate the carbonate concentration in the ocean. Schwieterman et al. (2019a) assumed $\Omega_{\text{cal}} = 1$, but calcite may need to be supersaturated ($\Omega_{\text{cal}} \sim 10\text{--}20$) for abiotic precipitation to occur.

Furthermore, over Earth's history, the calcite concentration has varied from $[\text{Ca}^{2+}] = 10^{-2}$ to 3×10^{-1} mol/kg (Halevy & Bachan 2017). We therefore tune $\Omega_{\text{cal}}/[\text{Ca}^{2+}]$ to match the observed total dissolved inorganic carbon in the surface oceans for pre-industrial conditions (see Table A1).

This tuning approach requires justification, as our model represents an Earth without oxygenic photosynthesis or complex skeletal organisms, analogous to conditions during the Archean and early Proterozoic eons. In the modern ocean, carbonate precipitation is predominantly biogenic (Chave & Suess 1970; Bialik et al. 2022), though Bialik et al. (2022) estimate that abiotic aragonite precipitation accounts for approximately 15% of CO_2 efflux in oligotrophic regions where surface waters remain supersaturated with respect to calcium carbonate. However, evidence supports that abiotic carbonate precipitation processes, while kinetically slower than biogenic precipitation, can achieve similar steady-state DIC concentrations over geological timescales. Laboratory experiments show that abiotic calcite precipitates at rates two to five orders of magnitude slower than biotic calcite (Carpenter & Lohmann 1992), but given billion-year timescales, kinetic limitations become less constraining.

Furthermore, geological evidence supports widespread abiotic carbonate precipitation in Earth's early history. The Precambrian geological record shows extensive carbonate platform deposition (Grotzinger 1989; Grotzinger & Kasting 1993; Grotzinger & James 2000), including meter-thick beds of fibrous calcite and aragonite precipitated directly on the Archean seafloor (Sumner & Grotzinger 1996). Sumner & Grotzinger (1996) argued that high rates of abiotic precipitation in Archean oceans were facilitated by elevated Fe^{2+} concentrations in anoxic seawater, which paradoxically promoted aragonite precipitation while inhibiting calcite nucleation. This geological evidence demonstrates that abiotic processes can generate substantial carbonate deposits, supporting our assumption that calcite saturation is achievable without biology.

We find that the optimal $\Omega_{\text{cal}}/[\text{Ca}^{2+}]$ to match pre-industrial DIC is 408.1 kg/mol. Recent spatial mapping of global calcite saturation of present-day oceans shows an average $\Omega_{\text{cal}} = 4.3$ (Shaik et al. 2025), and the present-day $[\text{Ca}^{2+}]$ is 10.28 mmol/kg (Halevy & Bachan 2017), corresponding to a present-day ratio of $\Omega_{\text{cal}}/[\text{Ca}^{2+}] = 398$. Conservatively estimating that a supersaturation factor of $\Omega_{\text{cal}} = 20$ is required for abiotic carbonate precipitation, our calibrated $\Omega_{\text{cal}}/[\text{Ca}^{2+}]$ corresponds to a calcite concentration of 49 mmol/kg. We

discuss the possible limitations of this tuning approach in Section 4.3.

We model this chemical system using the following equations adopted from Pilson (2012):

$$k_e = \frac{[\text{H}^+][\text{HCO}_3^-]}{(\text{CO}_2)_{\text{aq}}}, \quad (25)$$

and

$$k_f = \frac{[\text{H}^+][\text{CO}_3^{2-}]}{[\text{HCO}_3^-]}. \quad (26)$$

Since $k_e/k_f = [\text{HCO}_3^-]^2/([\text{CO}_3^{2-}][\text{CO}_2])$, we can combine these rate constant equations to solve for the concentration of bicarbonate:

$$[\text{HCO}_3^-] = \sqrt{(\text{CO}_2)_{\text{aq}}[\text{CO}_3^{2-}] \times \frac{k_e}{k_f}}. \quad (27)$$

Finally, we can solve for the concentration of $[\text{H}^+]$ by taking

$$[\text{H}^+] = \frac{K_{sp}[\text{HCO}_3^-]}{[\text{CO}_3^{2-}]}, \quad (28)$$

where $\text{pH} = -\log_{10}[\text{H}^+]$.

2.6. Surface Albedo

The surface albedo of the planet in our model consists of contributions from the ground and atmospheric water vapor clouds. Based on previous work (Driscoll & Bercovici 2013), we simulate the evolving total planetary surface albedo A_T by allowing the ground albedo A_g and cloud fraction ϕ to vary with time so that

$$A_T = A_g(1 - \phi) + A_{cl}\phi. \quad (29)$$

We assume that our Earth-like water vapor clouds have an albedo of $A_{cl} = 0.89$, which represents an average albedo of thick and thin clouds (de Pater & Lissauer 2010; Driscoll & Bercovici 2013). We assume a constant fraction of the atmospheric H_2O reservoir condenses into clouds, and tune the wavelength-independent cloud opacity pressure to ensure we match the PIE surface temperature at 4.5 Gyr. As in Driscoll & Bercovici (2013), we then calculate the cloud reflectivity fraction using the two-stream Eddington approximation,

$$\phi = \frac{\gamma(1 - e^{-2\beta_{\tau,cl}})}{1 - \gamma^2 e^{-2\beta_{\tau,cl}}}, \quad (30)$$

with $\tau_{cl} = 4800$ Pa as the constant cloud opacity pressure and scattering constants

$$\gamma = \frac{\beta - 2(1 - \bar{w})}{\beta + 2(1 - \bar{w})} \quad (31)$$

and

$$\beta = \sqrt{3(1 - \bar{w})(1 - \bar{w}g_w)}, \quad (32)$$

where \bar{w} is the single-scattering albedo $1 - \bar{w} = 1 \times 10^{-7}$ and $g_w = 0.74$ is the asymmetry factor (Hashimoto & Abe 2001). Given this cloud model is highly simplified, we tune the parameters to match pre-industrial Earth conditions. In other words, we will *not* attempt to match the pre-industrial Earth cloud coverage with the model.

The ground albedo A_g consists of contributions from surface rock (x_r), ocean (x_{oc}), and ice (x_i) fractions, where

$$A_g = x_r A_r + x_{oc} A_{oc} + x_i A_i. \quad (33)$$

We take the albedo of rock to be $A_r = 0.17$ (Kaltenegger et al. 2007; Driscoll & Bercovici 2013), the albedo of ocean water to be $A_{oc} = 0.1$ (de Pater & Lissauer 2010; Driscoll & Bercovici 2013), and the albedo of ice to be $A_i = 0.6$ (Kaltenegger et al. 2007; Driscoll & Bercovici 2013). As in Driscoll & Bercovici (2013), we assume a conical ocean basin with a slope angle of $\theta_{oc} = 0.06188^\circ$, which is calibrated to give $x_{oc} = 0.71$ when $w_{\text{ocean}} = 1.4 \times 10^{21}$ kg. To model ice growth, we include the simple relation from Driscoll & Bercovici (2013), which gives $x_i = x_{i,\text{max}} \times (1 - x_{oc}) \times (x_{oc}/x_{oc,0})$, where $x_{i,\text{max}} = 0.12$ is the maximum ice fraction, $(1 - x_{oc})$ is the fraction of land, and $x_{oc,0}$ is the present-day ocean fraction of 0.71.

Previous work has established that habitability requires only some amount of liquid water on the planetary surface (Kasting et al. 1993), and that global average surface temperatures can be meaningfully compared to spatially-resolved three-dimensional climate states when assessing habitability thresholds (Charnay et al. 2013; Arney et al. 2016). Charnay et al. (2013) demonstrated through 3D general circulation modeling that complete glaciation (e.g., a “snowball” Earth) likely does not occur until global average surface temperatures fall below 240 K, owing to spatial heterogeneity in ice coverage and meridional heat transport that maintains liquid water reservoirs at the equator. We therefore allow $x_i = 1.0$ when the global average surface temperature is ≤ 240 K, though like Driscoll & Bercovici (2013) our model does not currently handle transitions between global glaciation phases and $x_{i,\text{max}}$.

2.7. Climate

Planetary surface temperature is related to surface and atmospheric characteristics as well as the radiation received from the star. We determine surface temperature by calculating thermal equilibrium between the absorbed shortwave radiation (ASR) and the outgoing

long-wave radiation (OLR). OLR is a function of surface temperature and the atmospheric abundances of water vapor and CO_2 , while ASR is additionally a function of the total albedo, incoming stellar flux, and effective stellar temperature.

To calculate ASR and OLR, we use the `clima` module of the `Photochem` software package [Wogan et al. \(2025b\)](#). `clima` uses standard two-stream methods ([Toon et al. 1989](#)) to solve the radiative transfer equations, incorporating opacity tables to simulate continuum UV absorption, Rayleigh scattering, and collision-induced absorption, while accounting for line absorption with the correlated-k method. This approach explicitly captures the wavelength-dependent absorption and scattering processes that gray atmosphere models cannot. `clima` has been benchmarked against other community radiative transfer codes including SOCRATES ([Wolf et al. 2022](#)), ExoRT ([Wolf et al. 2022](#)), SMART ([Meadows & Crisp 1996](#)), and the radiative transfer code used by [Kopparapu et al. \(2013\)](#), demonstrating good agreement across a range of atmospheric compositions and stellar spectra. Furthermore, the code reproduces the observed pressure-temperature profiles of Venus, Earth, Mars, Jupiter and Titan ([Wogan et al. 2025b](#)).

To resolve 1-D atmospheric structure, we use the mode of `clima` that assumes an isothermal stratosphere above a convective troposphere with a pseudo-moist adiabat. The stratospheric temperature is estimated via the skin temperature for an assumed bond albedo, A_b . As in any 1-D climate model, `clima` has a limited ability to self-consistently calculate the radiative impact of clouds. As a result, we follow previous work (e.g., [Kopparapu et al. 2013](#)) and “paint” them on the surface by incorporating them into the total surface albedo, which is an input to the radiative transfer calculation (see Section 2.6).

Using the stellar evolution module in `vPLanet` ([Baraffe et al. 2015](#)), we calculate the evolving incoming stellar flux (F_\star) and temperature (T_\star) as a function of time. To determine the top-of-atmosphere solar flux, `clima` calculates a black-body distribution corresponding to T_\star . This ensures that ASR accounts for how the evolving Sun impacts wavelength-dependent atmospheric opacity. Rather than calling the full radiative transfer calculation at every timestep, which would be computationally prohibitive for billion-year integrations, we precompute a grid of OLR and ASR values as functions of surface temperature, atmospheric CO_2 partial pressure, the total H_2O surface inventory, stellar flux, stellar effective temperature, and surface albedo.

The grid spans surface temperatures from 100 K to 500 K (41 points, spaced at 10 K intervals), CO_2 partial pressures from 10^{-6} to 10^4 bar (21 points, logarith-

mically spaced at 0.5 dex intervals), H_2O total surface pressures from 10^{-3} to 10^4 bars (15 points, logarithmically spaced at 0.5 dex intervals), stellar flux from 800 to 2000 W/m^2 (13 points, spaced at 100 W/m^2 intervals), surface albedoes of 0.0, 0.1, 0.3, 0.5, 0.7, and 0.9 (6 discrete values), and stellar effective temperatures from 5000 to 6000 K (5 points, spaced at 250 K intervals). At each model timestep, we pass the current values of T_{surf} , $p\text{CO}_2$, total surface water inventory (in bars), stellar flux (F_\star), A_T , and stellar effective temperature (T_\star) to a multidimensional linear interpolation routine that returns the corresponding OLR and ASR from the pre-computed grid. The complete grid contains approximately 9.7 million pre-computed atmospheric states.

We then use Brent’s method ([Brent 2013](#)) to iteratively solve for the equilibrium surface temperature where ASR equals OLR, using a bracket of [100, 600] K and a tolerance of 2×10^{-12} . Once convergence is achieved, we pass the solved T_{surf} back to `vPLanet` to update all temperature-dependent parameters. This grid-based approach maintains the approximate accuracy of full radiative transfer calculations ($<\sim 1$ K error) while reducing computational cost by approximately three orders of magnitude, enabling efficient exploration of long-term planetary evolution.

In `clima`, we parameterize the H_2O inventory as a pressure column (in bars) representing the total surface water reservoir (w_{surf} converted to an equivalent pressure). `clima` internally partitions the combined surface reservoir between atmospheric vapor (limited by saturation vapor pressure at each vertical level) and condensed phases, capturing the coupled radiative-thermodynamic effects of water vapor feedback. Once a steady-state climate is computed, we extract the atmospheric composition using `clima`’s vertically-resolved solution. We extract the surface water vapor mixing ratio and the total surface pressure from the interpolated grid output, which represent `clima`’s self-consistent partitioning of water between the atmosphere and ocean when accounting for temperature stratification throughout the atmospheric column. This more physically accurate partitioning refines our initial surface-only estimates described in Sections 2.4. We recalculate w_{atm} , w_{ocean} , c_{atm} and c_{ocean} to match `clima`’s atmospheric state, ensuring that the water distribution used in subsequent carbon cycle and thermal evolution calculations remains consistent with the radiative transfer solution.

2.8. Reflected Light Spectra

We use the `PICASO` code ([Batalha et al. 2019](#)) to compute synthetic HWO reflected light spectra (0.2–2.0 μm) for the true Earth and the abiotic Earth’s atmospheric

state after 4.5 Gyr. We use a set of $R = 15,000$ resampled opacities archived on Zenodo (Wogan et al. 2025a), derived from a similar set of HITEMP (Rothman et al. 2010) and HITRAN (Gordon et al. 2017) opacities used by `c1ma` for climate calculations (Section 2.7). The opacity database accounts for line absorption from the following relevant species: CO₂, H₂O, O₂, O₃, and CH₄. Relevant CIA partners include CO₂-CO₂, H₂O-H₂O, H₂O-N₂, N₂-N₂, N₂-O₂, and O₂-O₂. `PICASO` also includes Rayleigh scattering for all specified molecules.

We compute two reflected light spectra: (1) a realistic modern Earth spectrum using temperature and mixing ratio profiles from the Intercomparison of Radiation Codes in Climate Models (ICRCCM) case 62, which represents the averaged mid-latitude Earth during the summer months (Lincowski et al. 2018), and (2) an abiotic Earth spectrum using the `vPLanet` atmospheric state after 4.5 Gyr, which includes only CO₂ and H₂O as greenhouse gases along with 1 bar of N₂. For both spectra, we input an expected surface albedo of 0.14 (without clouds) and include a cloud deck. We model clouds as a single gray deck extending from 0.6 to 0.7 bar with an optical depth of 10, a single-scattering albedo of 0.99, and an asymmetry parameter of 0.85. We compute both cloudy and cloud-free spectra and weight them by a cloud fraction of 50% to approximate Earth’s observed cloud coverage. Both calculations assume solar illumination at quadrature (90° phase angle) and are binned to $R = 140$.

The ICRCCM Earth reference profile has been re-interpolated onto the `vPLanet` pressure grid to enable direct comparison. The `vPLanet` grid has a surface pressure of 1.016 bar compared to the ICRCCM value of 0.989 bar, representing a difference of approximately 0.03 bar, or 3% higher surface pressure. The top-of-atmosphere (TOA) extends to 1.1×10^{-5} bar in the `vPLanet` grid versus 1×10^{-7} bar in the original ICRCCM profile. The number of atmospheric layers differs as well, with 51 layers in the `vPLanet` grid compared to 63 layers in the original ICRCCM profile. These differences are minor – the 3% surface pressure difference causes negligible changes in atmospheric column density, and the higher TOA cut-off removes only the uppermost stratosphere and mesosphere, which are optically thin and contribute minimally to the spectrum. The temperature-pressure profile, water vapor distribution, and other trace gas abundances have been linearly interpolated in log-pressure space to preserve the atmospheric structure of the original ICRCCM profile.

2.9. Initial Conditions

Our model requires the initialization of key parameters, including those describing the initial conditions of the interior and the surface volatile inventories. Here we briefly describe how we initialized our model. Model evolution is initialized at 50 Myr following the magma ocean phase. Most other initial values are calibrated to match the relevant measurements of the pre-industrial Earth. Though the model evolution is largely insensitive to the initial CO₂ and H₂O inventories, we base the total initial masses of volatiles on previous work.

To compute a plausible evolutionary model for Earth, we optimized 16 initial conditions and constants of the interior (given in Table 2) to reproduce Earth’s present-day interior properties (given in Table 1). To perform the optimization, we assumed a Gaussian likelihood function based on the mean and uncertainty of each output parameter, and minimized the negative log-likelihood using the Nelder-Mead simplex algorithm (Nelder & Mead 1965) implemented in `SciPy` (Jones et al. 2001). Due to the multi-modal nature of likelihood space, we initialized the optimization at 200 different starting locations uniformly sampled over a wide parameter range, and selected the maximum likelihood fit out of all runs that converged.

As in Seales & Lenardic (2020) we initialize our model with 2 terrestrial oceans (TOs) of water. From Sleep & Zahnle (2001), we assume that Earth’s total initial CO₂ inventory is 1.1×10^{21} kg. Initially, to partition the volatiles between the interior and surface reservoirs, we follow estimations of the primordial Earth atmosphere immediately following the solidification of the magma ocean. Elkins-Tanton (2008) predicts primordial Earth CO₂-H₂O atmospheres ranging from 90–3350 bars. Consistent with the lower end of these estimates, we initialize the surface with 5 bars of CO₂ and 530 bars of H₂O (2 T.O.) for a combined primordial atmosphere of 535 bars.

Though the magma ocean phase may conclude with a higher surface inventory of CO₂, through initial model testing we found that the $p\text{CO}_2$ evolution is largely independent of the initial atmospheric carbon inventory. This model behavior occurs because the seafloor weathering flux (Equation [8]) directly depends on plate speed and $p\text{CO}_2$ relative to the present-day, which would be very large immediately following the magma ocean phase. As a result, basaltic seafloor weathering is expected to be efficient enough to draw nearly all of the CO₂ out of the atmosphere. Therefore, we initialize the model with 5 bars to maximize model stability – all CO₂ reservoirs must initially contain non-zero mass, and the remaining CO₂ is split between the plate and the mantle.

In summary, our model couples interior thermal evolution (`ThermInt`, `RadHeat`), volatile cycling (carbon and water), ocean chemistry, and climate (`clima`) into a unified framework. We track CO_2 and H_2O masses across mantle, ocean, and atmospheric reservoirs with fluxes controlled by plate tectonics and weathering. Key model features include a radiogenically enriched BMO, water-dependent mantle viscosity, calcite-saturated ocean chemistry, and evolving planetary surface albedo from ground and cloud contributions. We initialize the model as described above, then evolve the system forward 4.5 Gyr, optimizing 17 interior parameters to match 19 pre-industrial Earth properties.

3. RESULTS

In this section, we show that the whole-planet model successfully reproduces the pre-industrial Earth after 4.5 Gyr of model evolution. We also generate a corresponding reflected light spectrum to compare against that of a realistic, cloudy Earth. Model results and comparisons to measured values within uncertainties are summarized in Table 3, and in Table 2 we report the calibrated interior parameter values following our optimization procedure described in Section 2.9.

In Figure 3, we show the incoming solar flux at the planet as a function of time. Using the Baraffe et al. (2015) model, the evolving solar flux starts at 943 W/m^2 ($\sim 0.7L_\odot$) and reaches 1370 W/m^2 ($1.0L_\odot$) by 4.5 Gyr. The final incoming stellar flux is thus consistent with its present-day value. Furthermore, the early stellar flux is consistent with predictions of other stellar evolution models used to model the faint young Sun (Sagan & Mullen 1972; Newman & Rood 1977; Gough 1981).

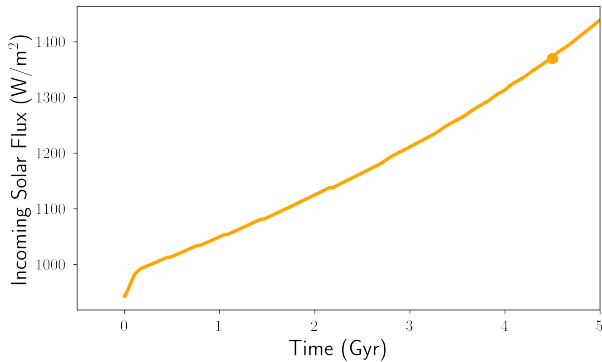


Figure 3. Incoming solar flux evolution with time, where the dot at 4.5 Gyr represents the present-day value.

Figure 4 shows the evolution of bulk planetary parameters including surface temperature, total albedo (ground and clouds), atmospheric $p\text{H}_2\text{O}$, and atmo-

spheric $p\text{CO}_2$. By 4.5 Gyr, the planet surface temperature reaches 286.9 K (a), the ground albedo (solid line) is 0.14 while the total albedo including clouds (dashed line) is 0.198 (b), the atmospheric $p\text{H}_2\text{O}$ is 1632 Pa with an assumed relative humidity of 100% (c), and the atmospheric $p\text{CO}_2$ is 28.2 Pa (d). The atmospheric water vapor abundance (c) shows a strong relationship with planetary temperature (a) due to the efficiency of OLR absorption and strong temperature-dependence of saturation vapor pressure. After 4.5 Gyr, our model predicts that the total degassing flux of CO_2 is 1.2 Tmol/yr and that of H_2O is 10 Tmol/yr – both are reasonably close to the present-day observations of 1–5 and 11 Tmol/yr, respectively.

At the start of the evolution, following a brief (~ 100 Myr) equilibration period, the planet is relatively cold, with $T_{\text{surf}} = 272 \text{ K}$, which is still well above the 240 K threshold for complete glaciation (Section 2.6). In response, the weathering is low while the degassing flux is high, allowing the atmospheric CO_2 abundance to spike to ~ 1 bar 100,000 years after model initialization. As the planet warms, weathering is enhanced and the carbon sinks begin to overwhelm the sources, resulting in a gradual decrease in $p\text{CO}_2$. Initial oscillations in CO_2 (< 5 Myr) occur due to a disequilibrium between CO_2 partitioning and the rapidly cooling mantle and surface temperatures. The final state of the model is ultimately insensitive to these initial model conditions. Furthermore, the transition between magma ocean solidification and the onset of plate tectonics is poorly understood, and modeling this transition falls outside the scope of this work.

The total albedo includes contributions from the ground and clouds, and is therefore higher. Clouds are tuned to match the PIE temperature. From tuning the constant cloud opacity pressure, we find a total albedo of 0.198 corresponding to a cloud fraction of 8%. We note that this is likely an unrealistically small cloud fraction for the PIE, most likely due to our simplified cloud implementation (see Section 4.5).

Figure 5 shows the evolution of the surface and mantle water budgets (a), the aqueous CO_2 concentration (b), ocean pH (c), and the surface ocean's total dissolved inorganic carbon (DIC) concentration (d). We initialize the surface with 2 TOs, resulting in 1 TO in the mantle after 4.5 Gyr. Using Henry's law, we calculate an aqueous CO_2 concentration of $10.8 \mu\text{mol/kg}$ by 4.5 Gyr (b). Assuming a constant carbonate concentration based on the abiotic calcite budget, we obtain a pH of 8.28 after 4.5 Gyr (c). Finally, the total dissolved inorganic carbon (DIC) at the ocean's surface is $1919 \mu\text{mol/kg}$ after 4.5 Gyr (d). Ocean pH exhibits strong

Parameter	Value
Initial ^{40}K power in the mantle	5.14×10^{13} W
Initial ^{40}K power in the core	4.05×10^{13} W
Initial ^{232}Th power in the mantle	7.01×10^{12} W
Initial ^{232}Th power in the core	1.30×10^{11} W
Initial ^{238}U power in the mantle	1.04×10^{13} W
Initial ^{238}U power in the core	1.0×10^{11} W
Initial ^{235}U power in the mantle	1.66×10^{13} W
Initial ^{235}U power in the core	4.68×10^{11} W
Initial mantle temperature	2700 K
Initial core temperature	5700 K
Melt eruption efficiency	0.01 [n.d.]
Core liquidus depression	4.04×10^{-4} K
Lower/upper mantle viscosity ratio	1.5 [n.d.]
Depression of mantle viscosity activation energy due to water	9.642×10^6 K
Viscosity activation energy	2.64×10^5 J mol ⁻¹
Upper mantle thermal conductivity	4.24 W/m/K

Table 2. Initial conditions and constants of the interior Earth model. Core radiogenic power includes BMO contribution (see Section 2.1).

temperature-dependent behavior, while the DIC evolution tracks closely with the atmospheric CO₂ evolution. When the atmospheric CO₂ abundance is initially high (Figure 4, d), the aqueous CO₂ concentration is also high (Figure 4, b). Following model equilibration, as atmospheric CO₂ abundances sharply increase prior to 1 Gyr, the aqueous CO₂ concentration rises to 2×10^{-2} mol/kg, and the ocean pH is ~ 6.6 , or 30× more acidic than present-day Earth oceans. As the atmospheric CO₂ content gradually wanes to PIE values, the aqueous CO₂ concentration and DIC follow suit, resulting in increasingly alkaline oceans.

Figures 6 and 7 show the evolution of mantle and core properties, respectively. In panel (a) we show the temperature evolution of the mantle (T_M), upper mantle T_{UM} , lower mantle T_{LM} , core-mantle boundary (T_{CMB}), and core (T_C). In panel (b), we show the evolution of heat flow in the upper mantle (Q_{UM}), and the core-mantle boundary (Q_{CMB}), as well as the radiogenic heat flow in the mantle ($Q_{\text{Rad},M}$) and core ($Q_{\text{Rad},C}$). Panel (c) shows the changing boundary layer depths of the upper (δ_{UM}) and lower mantle (δ_{LM}), while panel (d) shows the viscosity of the upper (ν_{UM}) and lower mantle (ν_{LM}) with time. Finally, panel (e) shows the upper mantle melt fraction, and panel (f) shows the melt mass flux over geological time. By 4.5 Gyr, we confirm that T_{UM} , T_{CMB} , Q_{UM} , Q_{CMB} , ν_{UM} , ν_{LM} , F_{melt} , and mantle melt mass flux all match measurements of Earth properties within 1- σ of measurement uncertainties.

In Figure 7, we show the evolution of key core properties over time. Panel (a) shows the radius of the inner

core with time, and panel (b) shows the core buoyancy flux. Finally, panel (c) shows the magnetic moment in Earth units, and panel (d) shows the magnetopause radius in Earth units. For all properties shown in this figure, we note an interesting discontinuity that occurs ~ 4 Gyr. This feature represents inner core nucleation in the model, when light elements begin to be rejected from the solidifying inner core (Driscoll & Bercovici 2014). The thermal buoyancy flux of the core gradually decreases as the core cools (b). Once the inner core begins to solidify light elements are injected into the base of the liquid outer core, generating compositional buoyancy and boosting the total core buoyancy flux (b). This buoyancy injection into the outer core boosts the magnetic moment and magnetopause radius (c and d). All four core related properties in Figure 7 match the final expected values within 1- σ of the measurement uncertainties.

Table 3 summarizes our final model values for 19 pre-industrial characteristics and the deviation from the observed values in units of measurement uncertainty (σ). We emphasize that these “deviation” values assume normally distributed uncertainties, which may not be the case for all parameters under investigation. Rather, the values reported here are primarily for illustrative purposes to quantify how close the model matched observations. As such, negative deviations represent instances where our model underestimates the value of a given parameter compared to expectation, while positive deviations indicate when our model overestimates the expectation. For 17 out of 19 key parameters, our model

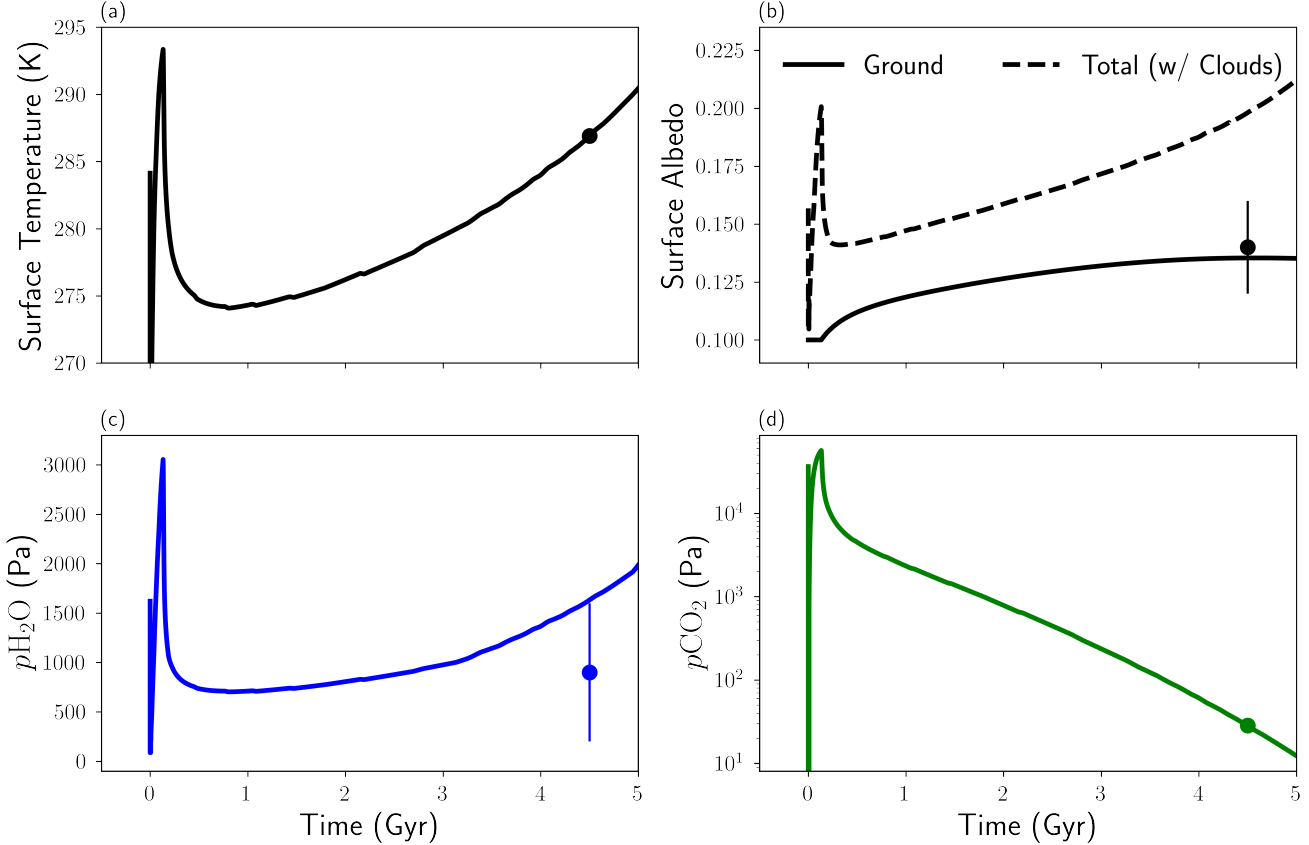


Figure 4. Some bulk properties of the abiotic Earth as a function of time. (a) Global average surface temperature warms as the star gradually brightens. (b) The ground albedo increases as dark ocean water subducts into the mantle and comparatively brighter land becomes exposed. Total albedo also increases as the warming planet’s atmosphere can hold more water vapor, and more clouds form. (c) As the planet warms, the atmosphere can hold more water and the H_2O partial pressure increases. (d) Finally, atmospheric CO_2 spikes early on when the planet is cold, and gradually decreases as weathering becomes more efficient on the warming planet. On all plots, dots represent measurements of PIE (4.5 Gyr) properties with uncertainties.

results are $\leq 1\sigma$ of the measured values. Of the 2 remaining parameters, $(\text{CO}_2)_{\text{aq}}$ is within 1.5σ , while the property for which our model shows the greatest deviation from truth is the ocean pH. We find that after 4.5 Gyr the ocean has a slightly more alkaline pH of 8.28, which represents a difference of 2.0σ relative to expectation. Since ocean pH is determined by the carbonate equilibrium system, this larger deviation from expectation for both ocean pH and $(\text{CO}_2)_{\text{aq}}$ can be attributed to our simplifying assumptions regarding calcite concentration. We discuss the implications of this assumption in Section 4.3.

Finally, as a proof of concept, in Figure 8, we compare reflected light spectra of a realistic cloudy Earth and a snapshot of the abiotic Earth after 4.5 Gyr (a), as well as their corresponding abundance profiles (b). Volume-mixing ratio profiles are shown in log-log space as a function of decreasing pressure in bars on the y-axis. While both atmospheres include CO_2 , H_2O , and N_2 , the

abiotic atmosphere lacks O_2 (and therefore O_3) and CH_4 . The lack of O_2 and O_3 contributes to the most significant differences in absorption between the two spectra. For example, in the near-UV $\sim 0.25 \mu\text{m}$, the true Earth spectrum shows absorption due to the O_3 Hartley band. In the visible, the Earth spectrum has absorption features at $\sim 0.6 \mu\text{m}$ due to the O_3 Chappuis band, and a prominent narrow-band feature at $\sim 0.76 \mu\text{m}$ due to the O_2 A-band. In the near-infrared, the Earth spectrum shows absorption at $\sim 1.27 \mu\text{m}$ due to the weak O_2 feature. Finally, the true Earth spectrum has ~ 2 ppm of CH_4 , which produces an absorption feature at $\sim 1.69 \mu\text{m}$ in the near-infrared. This low abundance results in a weak absorption feature that ultimately represents only a minor difference between the true and abiotic Earth spectra.

Figure 8b demonstrates some minor differences between the N_2 , CO_2 , and H_2O profiles. While the ICR-CCM atmosphere is 79% N_2 , the abiotic atmosphere

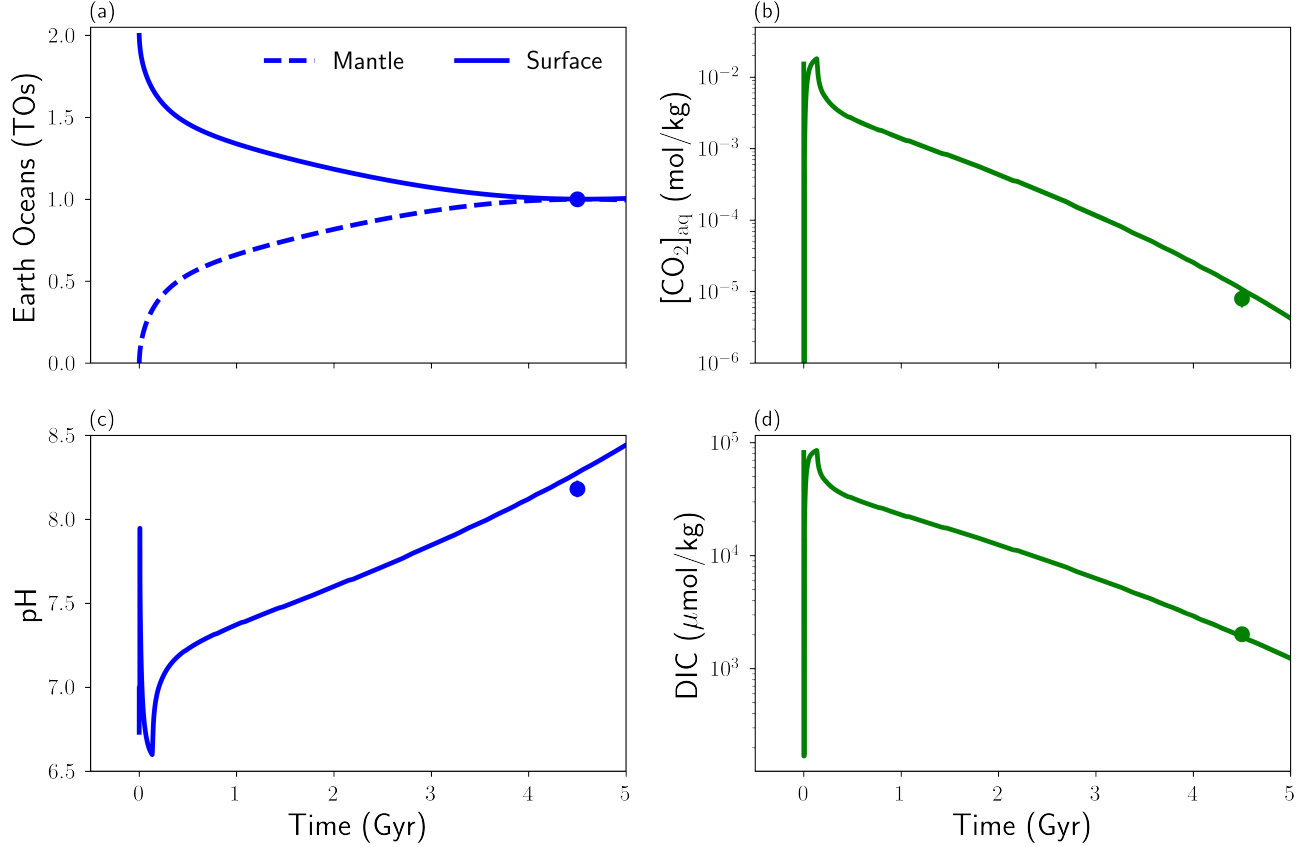


Figure 5. Properties of the ocean as a function of time. (a) After 4.5 Gyr, 1 TO has entered the mantle, ultimately leaving 1 TO on the surface. (b) The concentration of CO₂ in the oceans tracks closely with the atmospheric CO₂ inventory, following Henry's law. (c) Prior to equilibration, the pH initially spikes because of the initial concentration of carbonate and bicarbonate in the calcite-saturated oceans is also very high. Following equilibration, the pH gradually becomes more alkaline as the abundance of CO₂ in the atmosphere and ocean gradually decreases. (d) The total dissolved inorganic carbon at the ocean's surface, which includes aqueous CO₂, carbonate, and bicarbonate, tracks closely with the atmospheric CO₂ budget. On all plots, dots represent measurements of PIE (4.5 Gyr) properties with uncertainties.

has 1 bar to compensate for the lack of bulk O₂. Furthermore, the ICRCCM atmosphere was benchmarked to more recent terrestrial atmospheric abundances. As a result, the ICRCCM atmosphere has a higher CO₂ abundance of 330 ppm versus our 280 ppm. Lastly, though both water vapor profiles have similar near-surface abundances, our tropopause appears at a slightly lower pressure (and higher altitude) than the ICRCCM profile. This difference occurs for two reasons. First, the ICRCCM profile represents an average mid-latitude climate during the summer months whereas our profile represents a globally averaged profile. Second, `clima` estimates the location of the tropopause by calculating the atmospheric skin temperature rather than explicitly calculating the radiative-convective boundary. Nonetheless, these differences in the atmospheric profiles do not contribute to major differences in the resulting spectra – the weak CO₂ bands are insensitive to small differences

in abundance, and most spectral water vapor absorption occurs below the tropopause.

4. DISCUSSION

We have presented a coupled core-mantle-climate evolution model that reproduces 17 out of 19 properties of the pre-industrial Earth within 1- σ of measured values, and 2 ocean chemistry parameters within 2- σ of measured values. We have also shown that our model can be used to generate synthetic HWO-like reflected light spectra. Our findings suggest that the abiotic Earth could evolve to a similar state (in terms of global geophysics and climate) to present-day Earth without life, but without abundant atmospheric oxygen. In this section, we discuss the implications of key assumptions in our model, such as neglecting CH₄ and abiotic calcite saturation in the oceans. Finally, we dis-

Table 3. Abiotic Earth model values compared to pre-industrial Earth measurements. Model values are reported at 4.5 Gyr. The residual is calculated as (Model - Measured), and σ quantifies the deviation in units of measurement uncertainty (Residual / Uncertainty).

Properties	Measured Value	Model Value	Deviation [†] (σ)
Atmospheric CO ₂ ($p\text{CO}_2$)	28.4 ± 0.4 Pa	28.2 Pa	-0.50 σ
Atmospheric H ₂ O ($p\text{H}_2\text{O}$)	900 ± 700 Pa	1632 Pa	+1.05 σ
Surface temperature (T_{surf})	286.9 ± 0.1 K	286.9 K	+0.00 σ
Ground albedo (A_g)	0.14	0.14	+0.00 σ
Ocean mass (w_{ocean})	1.4×10^{21} kg	1.4×10^{21} kg	+0.00 σ
Oceanic (CO ₂)aq	8 ± 2 $\mu\text{mol/kg}$	10.8 $\mu\text{mol/kg}$	+1.40 σ
Total Dissolved Inorganic Carbon (DIC)	2000 ± 200 $\mu\text{mol/kg}$	1919 $\mu\text{mol/kg}$	-0.46 σ
pH	8.18 ± 0.05	8.28	+2.00 σ
Upper mantle temperature (T_{UM})	1587_{-34}^{+164} K	1562 K	-0.74 σ
Core-mantle boundary temperature (T_{CMB})	4000 ± 200 K	3889 K	-0.56 σ
Upper mantle heat flow (Q_{UM})	38 ± 3 TW	39 TW	+0.33 σ
Core-mantle boundary heat flow (Q_{CMB})	11 ± 6 TW	16 TW	+0.83 σ
Upper mantle viscosity (ν_{UM})	$(2.275 \pm 2.27) \times 10^{18}$ m ² s ⁻¹	2.867×10^{17} m ² s ⁻¹	-0.88 σ
Lower mantle viscosity (ν_{LM})	$(1.5 \pm 1.4) \times 10^{18}$ m ² s ⁻¹	5.4×10^{17} m ² s ⁻¹	-0.69 σ
Upper mantle melt fraction (F_{UM})	$11.5 \pm 3.5\%$	8.5%	-0.85 σ
Melt flux	$(1.3 \pm 0.8) \times 10^6$ kg/s	2.0×10^6 kg/s	+0.88 σ
Inner core radius (R_{IC})	1224.1 ± 0.1 km	1224.1 km	+0.00 σ
Magnetic moment	1.00 ± 0.05 E. Unit	1.01 E. Unit	+0.20 σ
Magnetopause radius	1.00 ± 0.02 E. Unit	1.00 E. Unit	+0.00 σ

NOTE—All measured values and uncertainties are detailed in Section 1.1, and summarized in Table 1. [†]The values in this column assume normally distributed uncertainties, which may not be the case for all parameters. “Deviation” values reported here are primarily for illustrative purposes to quantify how closely the model matched observations.

cuss our findings in the context of the Gaia hypothesis and forecast future research directions.

4.1. Spectroscopic Predictions for HWO Observations

The atmospheric states produced by our coupled evolution model can generate realistic reflected light spectra suitable for comparison with future HWO observations (see Figure 8). The most significant spectral differences arise from the absence of biologically-mediated gases: the modern Earth spectrum exhibits strong absorption features from O₂, O₃, and CH₄, none of which appear in our abiotic atmosphere.

This comparison validates that our model produces realistic atmospheric states that can be propagated through radiative transfer codes to generate synthetic HWO observations. The abiotic spectrum represents the expected appearance of a habitable but lifeless Earth-like planet, establishing a null hypothesis against which to test biosignature detections. While both spectra show prominent H₂O and CO₂ features, only the biological Earth exhibits the O₂ (or O₃)/CH₄ disequilibrium signature that would constitute compelling evidence for mod-

ern Earth-like life (Meadows et al. 2018). Future parameter space explorations varying planetary properties and host star types will reveal the diversity of reflected light spectra representing abiotic habitable worlds, establishing the range of null hypothesis scenarios that HWO must discriminate from life.

4.2. CH₄ as a Greenhouse Gas

Our model establishes that the carbonate-silicate cycle can operate effectively to maintain habitable surface temperatures over geological timescales using only CO₂ and H₂O as greenhouse agents, without requiring additional radiative forcing from trace gases like CH₄. This finding has important implications for understanding both Earth’s climate history and the potential habitability of rocky exoplanets.

Abundant atmospheric CH₄ due to microbial life on the early Earth has been proposed as a solution to the faint young Sun paradox (Pavlov et al. 2000; Kharecha et al. 2005). Pavlov et al. (2000) showed that atmospheric CH₄ mixing ratios of 100–1000 ppmv, combined with elevated CO₂ levels, could maintain above-freezing

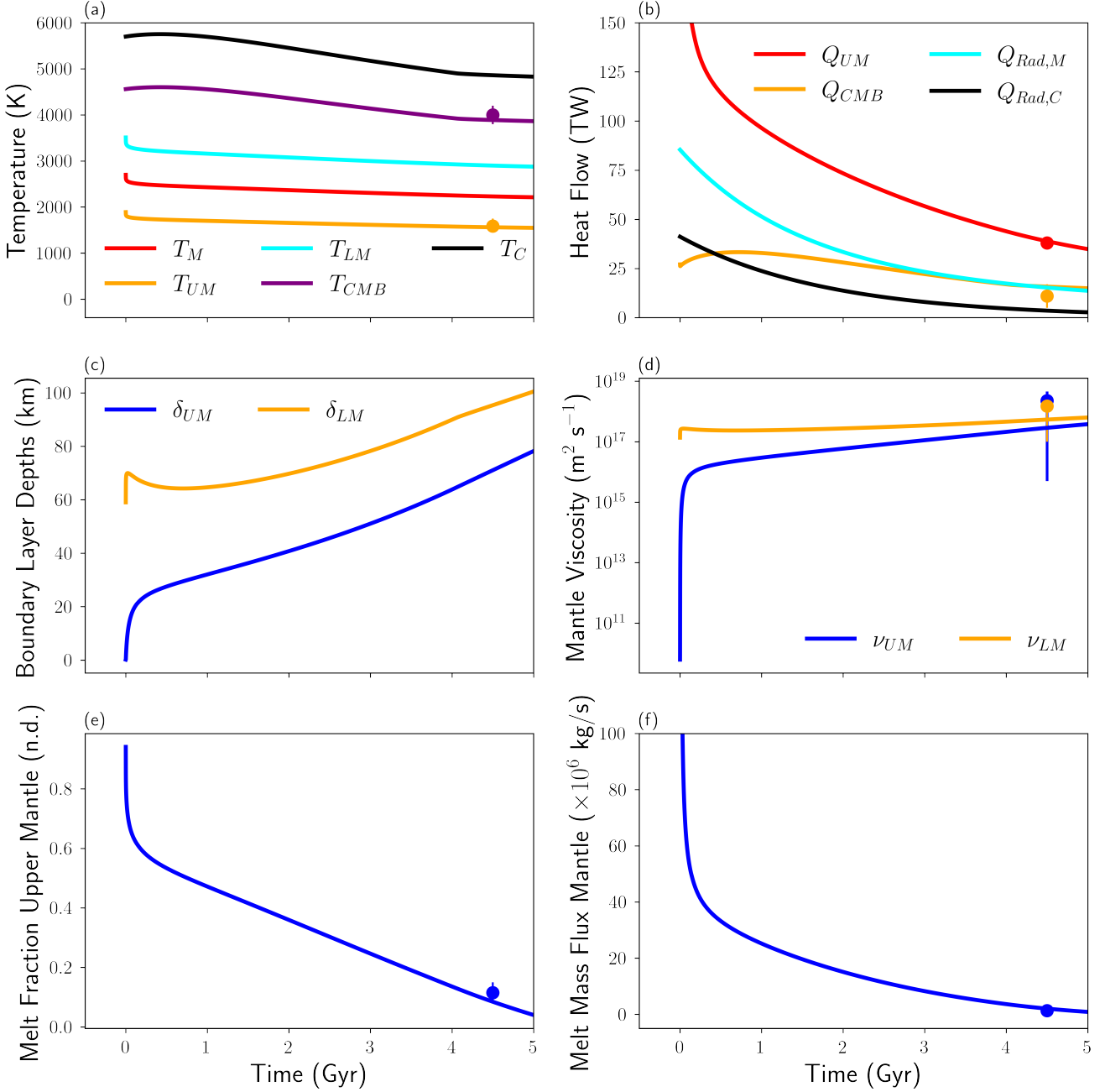


Figure 6. Key properties of the Earth's mantle through time. (a) The mantle and core gradually cool over time. (b) As the core and mantle cool, the heat flow across the upper mantle and the core-mantle boundary and the heat flow due to radiogenics in the core and mantle decrease. (c) Both the upper and lower mantle boundaries grow deeper as the core-mantle system cools and the mantle solidifies downwards. (d) The lower mantle is initially less viscous than the upper mantle. As water subducts into the cooling mantle, both the upper and lower mantle viscosities gradually increase. (e) As the interior cools, the upper mantle melt fraction rapidly decreases. (f) Similarly, the melt flux from the mantle also decreases as the mantle cools. On all plots where applicable, dots represent measurements of PIE (4.5 Gyr) properties with uncertainties.

temperatures despite 20–30% lower solar luminosity. While biological fluxes of CH_4 may have warmed Earth's climate in certain epochs – with some models suggesting temperature increases of 5–10°C from elevated methane

during the Archean (Roberson et al. 2011) – our results demonstrate that such biological enhancement is not necessary for maintaining habitability. An abiotic Earth

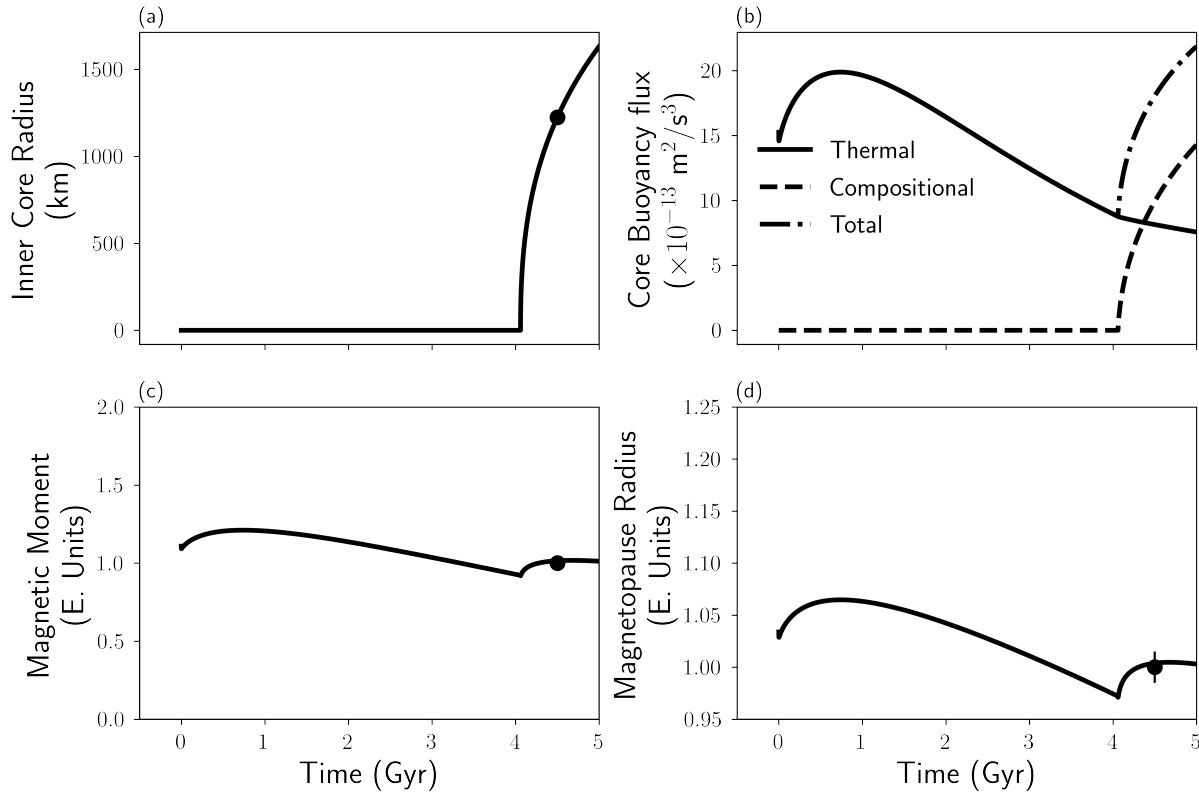


Figure 7. Key properties of the Earth's core through time. (a) Once the interior has sufficiently cooled, the inner core rapidly solidifies at ~ 4 Gyr. (b) The thermal buoyancy flux of the core gradually decreases as the core cools. Once the inner core solidifies and exsolves light elements, the compositional changes inject energy into the outer core and boost the overall core buoyancy flux. (c and d) The late energy increase in the outer core due to inner core solidification causes coinciding discontinuities in the magnetic moment and the magnetopause radius. On all plots where applicable, dots represent measurements of PIE (4.5 Gyr) properties with uncertainties.

can remain habitable through the $\text{CO}_2\text{-H}_2\text{O}$ greenhouse alone, provided the carbonate-silicate cycle operates.

Future work should nevertheless explore the sensitivity of climate evolution to low levels of abiotic CH_4 . Even modest trace gas abundances could influence atmospheric photochemistry and oxidation state. The atmospheric lifetime of methane depends strongly on photochemically generated hydroxyl radicals (OH^-) produced through water vapor photolysis (Pavlov et al. 2001). In an anoxic atmosphere without oxygenic photosynthesis, extended methane lifetimes could potentially allow greater accumulation than our simplified analysis suggests given sufficiently available OH^- . Additionally, planets orbiting M- and K-dwarf stars may experience different photochemical regimes due to their host stars' UV spectra, potentially affecting methane lifetimes and the viability of methane as a warming agent on abiotic worlds (Segura et al. 2005; Arney et al. 2016). Incorporating volcanic CH_4 outgassing coupled to mantle redox

state evolution would establish a more complete abiotic baseline for interpreting future observations of exoplanets orbiting different stars.

4.3. Abiotic Marine Calcite Budget

Tuning the calcite saturation and concentration to achieve the observed pre-industrial ocean DIC and approximate pH represents an oversimplification of the terrestrial carbon cycle, as demonstrated by the larger model disagreement for ocean pH (2.0σ) and aqueous CO_2 concentration (1.4σ). We tune the calcite saturation and concentration to match the observed total DIC (within 0.46σ), but this choice then constrains the carbonate ion concentration via the calcite saturation equation (Equation [24]), which in turn determines the partitioning among carbonate species through equilibrium constants (Equations [25], [26], and [27]), and ultimately fixes the pH. This cascade of constraints means that solely tuning calcite concentration to match total

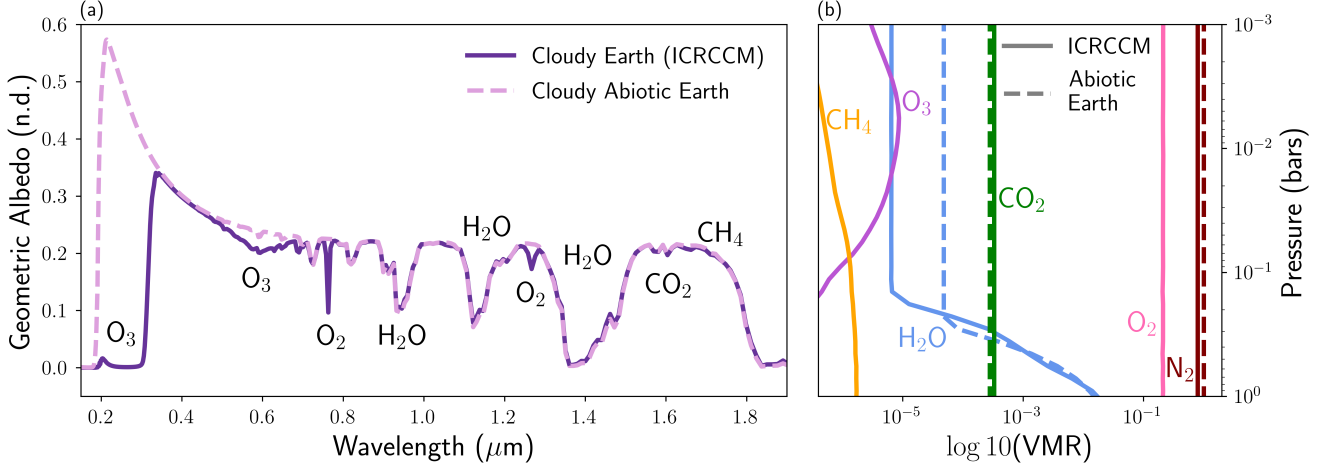


Figure 8. (a) A comparison of reflected light spectra for a realistic, cloudy Earth and the abiotic atmospheric state after 4.5 Gyr. The abiotic atmosphere lacks O₂ (and therefore O₃) and CH₄, contributing to differences in absorption. (b) A comparison of the input molecular abundance profiles used to generate each reflected light spectrum. We address minor differences between the CO₂, H₂O, and N₂ profiles in the accompanying text. Though the true profiles extend to a top-of-atmosphere pressure of 1×10^{-5} bars, we only show the surface to the upper stratosphere to better emphasize the differences in the water vapor profiles given the logarithmic scale.

DIC does not guarantee agreement with other observables that depend on the same carbonate chemistry, including pH and (CO₂)_{aq}.

The 2.0 σ pH offset highlights a fundamental limitation of our simplified ocean chemistry model: we assume calcite saturation and do not explicitly track total alkalinity as an independent variable, such as in Krissansen-Totton et al. (2021). In a more complete carbonate system, total alkalinity and DIC jointly determine pH and carbonate speciation. By fixing calcite concentration to match DIC, we implicitly constrain alkalinity through the carbonate equilibrium, removing a degree of freedom that would otherwise allow independent adjustment of pH.

The primary distinction between our abiotic model and a biologically mediated carbon cycle lies in how carbon is packaged for gravitational transport from the surface to the seafloor. The biological pump creates heavier, rapidly-sinking aggregates (marine snow, fecal pellets, shells) from organic and inorganic carbon (Paszow & Carlson 2012), allowing more carbon to reach the deep ocean before re-mineralization. Life effectively enhances gravitational export of carbon and influences the depth at which re-mineralization occurs. Organisms migrating vertically through the water column also transport metabolized carbon (Le Moigne 2019), but gravitational sinking dominates in modern oceans (Boyd et al. 2019; Nowicki et al. 2022; Siegel et al. 2023). In an abiotic ocean, gravitational settling of inorganic precipitates would still occur, but the size distribution, sinking velocities, and spatial patterns of carbonate formation

would likely differ from the biologically-mediated system.

Furthermore, it is unclear whether abiotic calcite is less thermodynamically stable than its biogenic counterpart. Zhuang et al. (2018) suggest that abiotic calcite is less stable than biogenic calcite due to lower crystallinity and activation energy, but Stalport et al. (2005) found that biologically precipitated calcite thermally degrades at temperatures approximately 40°C cooler than abiotic calcite, suggesting greater thermal stability of abiotic crystals at elevated temperatures. Pessimistically, these differing material properties combined with the orders-of-magnitude slower precipitation kinetics (Carpenter & Lohmann 1992) imply that achieving high calcite concentrations in an abiotic ocean may require either longer equilibration times or higher degrees of supersaturation than in living systems.

The extent to which a non-living planet could accumulate and maintain the calcite concentrations necessary to operate an effective carbonate-silicate thermostat remains an open question with implications for the long-term habitability of abiotic, Earth-like exoplanets. The calcite concentration directly impacts carbonate chemistry and thus the efficiency of oceanic carbon sequestration and weathering feedbacks. Future work should incorporate a more complete carbonate system with total alkalinity as a prognostic variable, following approaches like Krissansen-Totton et al. (2021). Additionally, systematic parameter space explorations should assess the sensitivity of ocean chemistry, atmospheric CO₂ regu-

lation, and surface temperature to variations in calcite concentration and alkalinity. Such studies would help establish the range of abiotic carbonate cycling rates compatible with maintaining temperate surface conditions on terrestrial planets over Gyr timescales.

4.4. Implications for the Gaia Hypothesis

Since its introduction by Lovelock & Margulis (1974), the Gaia hypothesis has spurred long-running debates over life's role in long-term climate stability (i.e., habitability). In evaluating Lovelock's original theory, Kirchner (1989) argues for re-categorizing Gaia into “weak” and “strong” variants – weak Gaia argues that interactions between living and abiotic processes have some stabilizing effect on the Earth; strong Gaia asserts that such interactions are the *most significant* process stabilizing Earth's climate. Strong Gaia proponents thus argue that life stabilizes the planetary thermostat by regulating temperature, atmospheric composition, and ocean chemistry to maintain conditions favorable to its survival and propagation (Lovelock & Margulis 1974; Lovelock 1983, 2000, 2016).

Generally, criticisms of the Gaia hypothesis acknowledge that life alters its environment, but point out that, despite some compelling examples, life's activities are not always favorable to its long-term survival. For instance, on the modern Earth, marine plankton “plunder” surface ocean nutrients, creating widespread biological deserts (Volk 2002; Kirchner 2003). Furthermore, the existential threat of anthropogenic climate change is a salient contemporary example of how biological activity can *disrupt* rather than stabilize the climate system (Kirchner 2002, 2003). These examples demonstrate that biological feedbacks are not intrinsically homeostatic.

More recently, modeling studies have investigated whether life can actively contribute to maintaining long-term planetary habitability. Nicholson et al. (2018) developed the ExoGaia model, which simulates how abiotic geochemistry and microbial metabolisms interact to influence surface temperature. They found that under stable conditions, microbial metabolisms can prevent planets from reaching inhospitable temperatures that would otherwise occur on their lifeless counterparts. Alcubes et al. (2020) extended this work by subjecting planets to three types of global climate perturbations, finding that planets with Gaian feedbacks are most resilient to global climate change, especially when changes are gradual. Together, these ExoGaia studies suggest that if life does emerge on a planet, it may under certain conditions evolve stabilizing feedbacks that enhance the long-term habitability of the host planet.

However, these models investigate whether life *can* stabilize planetary climate under a weak Gaia hypothesis, not whether life is *necessary* for climate stability as in the strong Gaia hypothesis. As further evidence against a strong Gaia mechanism, Kirchner (1989) identifies purely geophysical models that produce long-term climate stability without invoking life at all (Berner et al. 1983; Walker et al. 1981). Our results are in agreement with these models. We demonstrate that an Earth-like planet can maintain habitable surface temperatures over 4.5 Gyr of evolution (and longer) through abiotic processes alone, without requiring biological feedbacks for climate regulation.

The carbonate-silicate cycle, driven by the interplay between silicate weathering, volcanic outgassing, and ocean chemistry, provides a robust negative feedback that keeps atmospheric CO₂ and surface temperature within habitable bounds despite the Sun's luminosity increasing by approximately 30% over 4.5 Gyr. Critically, our model uniquely demonstrates this climate stability while self-consistently evolving all major planetary subsystems: the interior cools and outgassing rates decline; the magnetic dynamo weakens and the magnetopause contracts; ocean chemistry adjusts to changing atmospheric CO₂; and the incoming stellar flux steadily increases. Despite these dramatic changes, the coupled system maintains surface temperatures between 272–290 K throughout the evolution. This represents a more complete test of climate stability than previous models that considered the carbon cycle in isolation, as it demonstrates that the carbonate-silicate thermostat functions robustly even when embedded within a fully evolving planetary system with realistic feedbacks between interior, surface, atmosphere, and external forcing from the brightening Sun.

As discussed above, our model does simplify ocean chemistry, which biology enhances on the modern Earth (Section 4.3). However, the fundamental mechanism of climate stabilization – the temperature and CO₂ dependence of silicate weathering coupled to carbonate precipitation and subduction – operates independently of life. While life may affect the *spatial distribution* and *kinetics* of carbonate precipitation, these biological enhancements may not be *necessary* for long-term climate stability.

Our finding that life may not be a requirement of a habitable planet has important implications for understanding Earth's habitability and for predicting conditions on rocky exoplanets. The persistence of habitable conditions over geological time may not require life to actively regulate the climate, rather potentially emerging from volatile cycling between planetary reservoirs.

Habitable conditions may have been created on the early Earth by the abiotic carbonate-silicate cycle. Once life emerged, it may have developed stabilizing feedbacks as suggested by ExoGaia-type models (Nicholson et al. 2018; Alcabes et al. 2020), potentially altering weathering rates, ocean chemistry, and atmospheric composition. However, our results suggest that the underlying abiotic stabilization mechanism provided by the carbonate-silicate cycle can maintain habitability independently. While we cannot rule out that life enhances climate stability (weak Gaia), our results suggest that life is not a requirement of a habitable planet.

The implication that life may not be a requirement of a habitable planet raises a complementary question: given a habitable planet, how long does it take for life to emerge? On Earth, mineralogical evidence confirms that liquid water oceans existed as early as 4.4 Ga (Cameron et al. 2024), while the oldest widely accepted evidence for life – stromatolites from the Pilbara Craton – dates to 3.5 Ga (Walter et al. 1980). Though more ancient biogenic signatures have been proposed (and continue to be highly disputed), the stromatolite evidence provides a conservative estimate that abiogenesis occurred within approximately 900 Myr of ocean formation. It has been suggested that this relatively rapid emergence of life on Earth implies that abiogenesis may also be rapid on habitable exoplanets (Kipping 2025). Our results support this conjecture by showing how Earth could have been habitable but abiotic for billions of years, yet life still appeared relatively shortly after the appearance of habitable conditions. On the other hand, our model suggests that habitable surface conditions can persist for billions of years through purely abiotic mechanisms, potentially providing a prolonged “prebiotic window” during which the chemical building blocks of life could accumulate and undergo the reactions necessary for creating life.

Potentially habitable exoplanets observed by future missions may be captured at various stages of their prebiotic evolution: some may harbor early life similar to Earth at 3.5 Ga, while others could still be accumulating prebiotic chemistry despite having maintained habitable conditions for comparable or even longer durations. Indeed, our results suggest that rocky planets with plate tectonics, liquid water oceans, and silicate weathering can maintain habitable surface conditions over billion-year timescales without requiring biology. Thus, the mere presence of habitable conditions is not sufficient evidence that a planet is inhabited. Some worlds may remain prebiotic for prolonged periods, or never experience abiogenesis at all. Distinguishing inhabited from uninhabited-but-habitable worlds will therefore require (1) detecting disequilibrium biosignature gases (Love-

lock & Margulis 1974; Meadows et al. 2018) or surface features directly attributable to biological activity (Schwieterman et al. 2018), but also (2) a well-quantified abiotic baseline for the potential mimics of biosignature gases and surface biosignatures (e.g., Wogan et al. 2020; Krissansen-Totton et al. 2021).

4.5. Future Work

Our core-mantle-crust-climate model reproduces the conditions of the pre-industrial Earth without life, and provides a foundation for future studies aiming to simulate the evolving habitability of rocky exoplanets as well as the observable signatures of these states. However, we found that our simple cloud parameterization is likely insufficient to model realistic radiative forcing from clouds. We tuned a wavelength-independent cloud opacity pressure to match pre-industrial Earth surface temperature, resulting in an unrealistically low cloud fraction of 8% compared to Earth’s observed 67% average cloud coverage (Wielicki et al. 1996). This discrepancy arises because we “paint” clouds onto the surface rather than self-consistently calculating cloud formation and radiative effects within the atmospheric column (Fauchez et al. 2018). Future work should reconcile this inconsistency.

Our treatment of atmospheric processes spans a spectrum of physical fidelity. For surface temperature, atmospheric water vapor partitioning, and radiative transfer, we employ first-principles physics: `c1ima` solves the radiative transfer equations with wavelength-dependent opacities, while water vapor is constrained by the Clausius-Clapeyron relation at each atmospheric level. By contrast, clouds are parameterized – the cloud opacity scale and reflectance parameters are calibrated to reproduce the PIE’s cloud radiative effect, and are not derived from first-principles cloud microphysics.

While more sophisticated 1-D cloud treatments exist (Ackerman & Marley 2001; Zsom et al. 2012; Fauchez et al. 2018; Helling 2019; Windsor et al. 2023), implementing them would largely trade our current free parameters for others (e.g., sedimentation efficiency in microphysical models), without fundamentally resolving the uncertainties inherent to representing 3-D cloud processes in 1-D globally-averaged models. Clouds remain the dominant source of uncertainty in 3-D general circulation models due to the complex interplay of microphysics, planet-wide dynamics, and radiative transfer (Mauritsen et al. 2012; Vial et al. 2013; Way et al. 2018). For the purposes of investigating long-term planetary evolution across diverse parameter spaces, a more pragmatic approach is to acknowledge this uncertainty explicitly and marginalize over plausible cloud parame-

ter ranges when conducting broad explorations of Earth-like exoplanets. By varying our cloud opacity pressure and cloud albedo parameters across physically motivated ranges in future studies, we can assess how cloud radiative forcing uncertainties affect predicted habitability outcomes without requiring self-consistent calculations of cloud microphysics.

Further improvements to the model would ensure that it can capture additional feedback mechanisms of planets on diverse evolutionary paths. These improvements include incorporating additional volatile cycles and early Earth processes that affect the planet's initial conditions. Below we discuss potential model improvements and describe applications to exoplanet studies, which may include coupling our model outputs to 3-D general circulation models (GCMs) to better capture the complexity of surface processes like clouds and ice coverage.

Our model currently only handles CO₂ and H₂O cycling, which is a subset of Earth's geologically active volatiles. Following Krissansen-Totton et al. (2021), we assume that N₂ remains a bulk gas by setting it to a constant of 1 bar throughout the evolution. Future work should incorporate abiotic nitrogen cycling into our whole-planet model, as the abundance of atmospheric N₂ affects surface pressure and impacts the surface temperature of the planet via collision-induced absorption (Schwieterman et al. 2015) and pressure broadening of CO₂ and H₂O (Goldblatt et al. 2009). Furthermore, Lanneuville et al. (2018) showed that, in an abiotic context, the abundance of atmospheric nitrogen is highly dependent on surface and interior processes, suggesting this form of volatile cycling is ripe for inclusion in a whole-planet modeling framework.

While low abiotic CH₄ abundances likely do not directly contribute to greenhouse warming, methane nevertheless plays an important role in atmospheric chemistry and redox balance (Pavlov et al. 2001). The atmospheric abundance and lifetime of CH₄ depends on the availability of photochemically generated oxidants, which in turn depends on the planet's oxidation state, which is itself influenced by hydrogen escape to space (Catling et al. 2001; Zahnle et al. 2019). Atmospheric escape is therefore critical for determining both the feasibility of detecting abiotic methane and for interpreting CH₄ observations as potential biosignatures.

More broadly, atmospheric escape processes – particularly XUV-driven hydrodynamic and thermal escape – can substantially alter volatile inventories, atmospheric composition, and planetary oxidation state over Gyr timescales (Catling et al. 2001; Luger & Barnes 2015; Gialluca et al. 2024). This possibility is especially important for planets orbiting lower mass stars like M- and

K-dwarfs, which experience extended pre-main-sequence phases compared to G- and F-dwarfs, with high XUV fluxes that can drive significant atmospheric loss (Chadney et al. 2015; Atri & Mogan 2021). For example, on M-dwarf planets, preferential hydrogen escape oxidizes the atmosphere and potentially the mantle, affecting volcanic outgassing composition (the CH₄/CO₂ ratio), ocean chemistry, and the operation of the carbonate-silicate cycle (Gaillard et al. 2022; Schaefer et al. 2016).

Giant impacts during planetary formation and early bombardment can also drive atmospheric loss while simultaneously creating transient reduced atmospheres enriched in H₂ and potentially CH₄ (Zahnle et al. 2020). Future work should couple atmospheric escape and impact-driven atmospheric evolution to our model to track how early volatile loss shapes long-term habitability, particularly for planets around active K-dwarfs, which will be prime targets for atmospheric characterization with HWO (Arney 2019; Mamajek & Stapelfeldt 2023). Incorporating volcanic CH₄ outgassing, escape-driven oxidation, and impact-driven reducing conditions will establish a complete abiotic baseline against which to interpret methane detections in exoplanet atmospheres.

Our model is initialized after the magma ocean has crystallized. However, the magma ocean phase shapes the atmospheric composition and surface temperature of the early Earth. Volatiles incompatible with the magma ocean are released into the atmosphere (Elkins-Tanton 2012), and the rate at which the magma ocean cools may also contribute to whether or not a planet develops plate tectonics (Schaefer & Elkins-Tanton 2018). Thus, our model potentially underestimates the initial surface temperature and atmospheric volatile inventory of the planet, and does not account for how this early evolutionary process ultimately shapes Earth's habitability.

Though this work does not couple to the magma ocean, **VPLanet** already includes a magma ocean model. Carone et al. (2025) updated **Magm0c**, **VPLanet**'s magma ocean module, demonstrating good agreement with previous magma ocean models (Elkins-Tanton 2008; Nikolaou et al. 2019; Lichtenberg et al. 2021). Future work could integrate the **Magm0c** module into this whole-planet modeling framework, and continuously model the planet from the magma ocean phase into the solid mantle phase (e.g., Krissansen-Totton et al. 2021).

Finally, our 1-D model is not designed to account for complicated 3-D planetary phenomena like transitions to global glaciation states. Modeling a realistic ice-albedo feedback and snowball Earth transitions likely requires latitude-dependent insolation and heat transport that 1-D globally-averaged models cannot wholly

capture (Hoffman et al. 2017; Abbot et al. 2013; Rose et al. 2017; Wilhelm et al. 2022). Similarly, substantial discrepancies exist between 1-D and 3-D models regarding the height of cloud formation, cloud optical properties, and the climate impacts of clouds (Yang et al. 2016; Way et al. 2018; Komacek & Abbot 2019; Helling 2019).

Rather than attempting to fully incorporate these 3-D phenomena into our 1-D framework, we envision a complementary modeling approach. Our evolutionary model provides realistic time-dependent boundary conditions for GCM simulations: atmospheric composition, volatile inventories, interior heat flux, and incoming stellar flux at snapshots throughout planetary evolution. GCMs can then simulate the spatial climate patterns, ice coverage, cloud distributions, and circulation for these evolved atmospheric states (Wolf et al. 2022). Conversely, GCM-derived quantities – such as a spatially-averaged albedo that includes realistic cloud distributions, ice surface fractions, and meridional heat transport efficiencies – can inform improved parameterizations in 1-D evolutionary models without sacrificing the computational speed required to cover large parameter sweeps over Gyr-timescales. This iterative dialogue between complementary modeling approaches leverages the strengths of each: 1-D models are appropriate for long-term interior-atmosphere coupling, while 3-D models are useful for simulating spatially resolved climate states with realistic cloud and ice feedbacks. The integration of different modeling techniques will likely be essential for interpreting future observations of exoplanet atmospheres, and for predicting which planets are most likely to maintain habitable conditions over geological time.

With the additional model developments described above, a whole-planet framework could be used to assess abiotic mimics of life on Earth-like exoplanets. For example, an improved version of the model could build on the work of Krissansen-Totton et al. (2021) by assessing the evolution of abiotic O₂ in the atmospheres of exoplanets around Sun-like stars with a fully coupled core model. Our model would include the effect of an evolving core on the planet’s magnetosphere and the efficiency of hydrogen escape, which regulates the accumulation of abiotic O₂. The improved model could also be used to investigate the abiotic generation of other biosignature gases, like CH₄. This would expand on previous investigations of abiotic mimics by considering the evolution of the core-mantle system in addition to the star and planetary atmosphere.

In its current form, our model is well-poised for large parameter sweep explorations of Earth-like exoplanets throughout the HZs of FGK stars, both for the explo-

ration of habitable planet properties as well as the simulation of variations in observable signatures of habitability. For this Earth validation study, we solely show our model coupled to solar evolution, but the `vPLAnet` stellar model can simulate main sequence stars with masses up to $1.4M_{\odot}$. This mass range encompasses the Sun-like FGK stars that HWO will eventually target for observation.

Using preliminary HWO stellar target lists from Majek & Stapelfeldt (2023) and Tuchow et al. (2025), future work could simulate planets with the mass, radius, and tectonic regime of the Earth at various separations from FGK host stars. Since our coupled climate model performs full ASR and OLR calculations, it can be used to simulate the conditions at both the inner and outer edges of the HZ. At the inner edge, planets cease to be habitable when they enter the runaway greenhouse phase and at the outer edge, CO₂ scattering sets the maximum greenhouse limit (Kopparapu et al. 2013). To explore a wide range of planets, we can vary the initial CO₂ and H₂O inventories, as well as interior parameters like the radiogenics budget and the initial mantle and core temperatures. The unique luminosity evolution of each target star combined with various model parameters will shape the climate of a given planet over time, ultimately determining its potential long-term habitability.

Importantly, our evolutionary framework allows us to generate atmospheric states and synthetic HWO observations not just at a single endpoint, but at multiple snapshots throughout a planet’s history. A single Earth-like planet may exhibit dramatically different spectroscopic signatures at 1 Gyr, 3 Gyr, and 5 Gyr as its atmosphere, interior, and surface evolve in response to changing stellar forcing and volatile cycling. This application of our model would reveal how the stability of the Earth system is affected by different stellar types. For example, the comparatively slow luminosity evolution of K-dwarfs may promote long-term climate stability over the extended main sequence lifetime of these stars, while the relatively rapid brightening of F-dwarfs may challenge the climate stability of Earth-like exoplanets. The time-resolved atmospheric states across different evolutionary epochs can then be used to produce simulated HWO observations, providing insight on the range of spectral characteristics consistent with purely abiotic planetary conditions. This temporal dimension is crucial: the diversity of abiotic habitable worlds HWO will sample reflects not only variations in initial conditions and host star properties, but also the natural evolution of planetary systems captured at different ages.

5. CONCLUSIONS

Here we have presented a coupled core-mantle-crust-climate model that reproduces crucial geophysical, climate, and ocean properties of the pre-industrial Earth. Our model predicts that life is not required to maintain a habitable planet resembling Earth-like conditions. This work thus contributes to the ongoing debate regarding the Gaia hypothesis by suggesting that life and habitability may be somewhat decoupled.

In terms of future applications, our model is intended to be applied to the evolution of rocky exoplanets. Our model shows that the evolution of the planetary interior plays an important role in determining the long-term habitability of Earth-like exoplanets. Thus, including realistically evolving planetary interiors is a crucial aspect of whole planet modeling and should account for potentially non-Earth-like compositions in order to illuminate the potential equilibrium states of rocky planets.

Though exoplanet interiors themselves will likely never be directly observable, the effects of interior evolution are apparent in the composition of the atmosphere and the albedo of the surface environment, both of which HWO will observe on Earth-like planets around Sun-like stars via reflected light spectroscopy. We have demonstrated that atmospheric states from our model can generate realistic reflected light spectra that capture the key differences between inhabited and uninhabited worlds, establishing an abiotic baseline for biosignature interpretation. The model presented here is compatible with modeling the long-term habitability of theoretical exoplanets around key HWO targets. For quantifying the null hypothesis and establishing an abiotic baseline, additional model development is required. Nevertheless, our core-mantle-crust-ocean-atmosphere-stellar model represents significant progress towards the ambitious goal of whole-planet modeling, which itself is a key step towards advancing our search for life in the universe.

ACKNOWLEDGMENTS

We thank Joshua Krissansen-Totton, Jacob Lustig-Yaeger, and Thomas Quinn for their helpful comments, which improved this manuscript. Funding for S. G-J and A.M.M. was provided by the Exoplanet Spectroscopy Technologies Team at NASA Goddard, which is supported through the NASA Astrophysics Division Internal Scientist Funding Model. S. G-J was also supported by NASA award No. 80NSSC24M0049. R.K.B. was supported by NASA award No. 80NSSC24K0856, and R.G. was supported by NASA award No. 80NSSC23K0261. N.F.W. was supported by the NASA Postdoctoral Program. L.C. acknowledges support by the DFG priority programme SP1833 “Building a habitable Earth” Grant CA 1795/3.

Software: `vPLanet` (Barnes et al. 2020), `Clima` (Wogan et al. 2025b), `SciPy` (Virtanen et al. 2019; Virtanen et al. 2020)

APPENDIX

A. CONSTANTS

Table A1: All constants appear here in alphabetical order, with Greek letters appearing last. Values without units are denoted as non-dimensional (n.d.).

Symbol	Parameter	Value
a_1	saturation vapor pressure scaling parameter for silicate weathering	0.3 [n.d.]
a_2	plate velocity scaling parameter	5.38 [n.d.]
A_b	bond albedo	0.29 [n.d.]
A_i	ice albedo	0.6 [n.d.]
A_{oc}	ocean albedo	0.1 [n.d.]
A_r	rock albedo	0.17 [n.d.]
A_{Earth}	surface area of the Earth	$5.1 \times 10^{14} \text{ m}^2$
B	viscosity-melt reduction coefficient	2.5 [n.d.]
$D_{\text{H}_2\text{O}}$	bulk H_2O distribution coefficient	0.01 [n.d.]
E_a	silicate weathering activation energy	$42 \times 10^3 \text{ J/mol}$
$E_{a,\text{man}}$	mantle viscosity activation energy	$3 \times 10^5 \text{ J/mol}$
E_{max}	maximum erosion rate	$3.2 \times 10^{-10} \text{ m/s}$
f	fraction of subducted carbon that degasses	0.71202 [n.d.]
f_{cc}	fraction of Mg, Ca, K, and Na in the continental crust	0.08 [n.d.]
f_d	fraction of the upwelling mantle carbon that degasses	0.365 [n.d.]
f_h	mass fraction of water in the serpentized layer	0.03 [n.d.]
$F_{\text{sfw},0}$	present-day seafloor weathering flux	55, 454 mol/s
$F_{\text{weather},0}$	present-day silicate weathering flux	380, 257 mol/s
g	surface gravity of the Earth	9.8 m/s^2
k	thermal conductivity	4.2 W/m/K
L	present-day length of ocean trenches	$6 \times 10^7 \text{ m}$
L_w	latent heat of water	$2.469 \times 10^6 \text{ J/kg}$
\bar{m}_c	molar mass of CO_2	$44 \times 10^{-3} \text{ kg/mol}$
\bar{m}_{cc}	average molar mass of Mg, Ca, K, and Na	$32 \times 10^{-3} \text{ kg/mol}$
\bar{m}_w	molar mass of water	$18 \times 10^{-3} \text{ kg/mol}$
M_{man}	mass of the mantle	$4 \times 10^{24} \text{ kg}$
$p\text{CO}_{2,0}$	present-day partial pressure of atmospheric CO_2	33 Pa
$P_{\text{sat},0}$	present-day saturation vapor pressure	1391 Pa
$P_{\text{sat},\text{ref}}$	reference saturation vapor pressure	610 Pa
R_c	radius of Earth's core	$3481 \times 10^3 \text{ m}$

Continued on next page

Table A1: All constants appear here in alphabetical order, with Greek letters appearing last. Values without units are denoted as non-dimensional (n.d.). (Continued)

Symbol	Parameter	Value
R_g	universal gas constant	8.314 J/K/mol
RH	relative humidity	100%
R_{man}	radius of Earth's mantle	6371×10^3 m
Ra_{crit}	critical Rayleigh number	660 [n.d.]
S	salinity	35 ppt
S_0	solar constant	1369 W/m ²
$T_{\text{sat,ref}}$	reference saturation vapor temperature	273 K
$T_{\text{surf,0}}$	present-day surface temperature	285 K
v_0	present-day plate speed	1.58×10^{-9} m/s
V_{man}	volume of Earth's mantle	9.1×10^{20} m ³
ν_{ref}	reference kinematic mantle viscosity	8.544×10^8 m ² /s
$x_{i,\text{max}}$	maximum ice surface fraction	0.12 [n.d.]
$x_{l,0}$	present-day land fraction	0.29 [n.d.]
$x_{\text{oc},0}$	present-day ocean fraction	0.71 [n.d.]
α_1	strength of dependence of basalt carbonation on atmospheric CO ₂	0.25 [n.d.]
α_2	strength of the dependence of continental weathering flux on plate speed	1.5 [n.d.]
β_1	partial pressure of CO ₂ scaling parameter for silicate weathering	0.55 [n.d.]
β_2	scaling exponent of Rayleigh number for plate speed	1/3 [n.d.]
γ	viscosity-melt reduction coefficient	6.0 [n.d.]
δ	viscosity-melt reduction exponent	6.0 [n.d.]
$\Delta E_{\text{H}_2\text{O}}$	depression of mantle viscosity activation energy due to water	2.22×10^6 K/wt. frac.
κ	thermal diffusivity	1×10^{-6} m ² /s
ξ	viscosity-melt reduction coefficient	5×10^{-4} [n.d.]
ρ_{man}	density of the mantle ($M_{\text{man}}/V_{\text{man}}$)	4395 kg/m ³
ρ_r	density of regolith	2500 kg/m ³
σ_{SB}	Stefan-Boltzmann constant	5.67×10^{-8} W/m ² /K
τ_{cl}	cloud opacity pressure	4050 Pa
χ_d	water degassing efficiency	0.7156 [n.d.]
χ_r	water regassing efficiency	0.1248 [n.d.]
$\Omega_{\text{cal}}/[\text{Ca}^{2+}]$	marine calcite concentration	408.1 kg/mol

B. BMO RADIOGENIC HEATING CALCULATION

Here we provide a detailed derivation of the effective core radiogenic heating rate, which includes contributions from an enriched basal magma ocean (BMO) layer. We calculate the ⁴⁰K enrichment needed to generate up to 3.5 TW of heat in the core, which our model requires to match observed upper mantle heat flow.

B.1. Derivation of Effective Core Heating Rate

The core and BMO energy balances may be written as

$$-M_C c_C \dot{T}_C = Q_{\text{CMB}} + Q_{\text{rad,BMO}} - Q_{\text{BMO}}$$

and

$$-M_{\text{BMO}} c_{\text{BMO}} \dot{T}_B = Q_{\text{rad,C}} + Q_{iC} - Q_{\text{CMB}},$$

respectively, where M denotes mass, c denotes specific heat, \dot{T} denotes the time derivative of reservoir temperature, and Q denotes heat flow. The subscripts indicate the relevant reservoir: C denotes the core, CMB the core-mantle boundary, and BMO the basal magma ocean layer. Thus, $Q_{\text{rad,BMO}}$ represents the radiogenic heat flow in the BMO, and $Q_{\text{rad,C}}$ represents the radiogenic heat flow in the core. We neglect tidal heating, as it is not a significant source of internal heating for Earth (Ray et al. 1996). Adding these equations yields

$$-M_C c_C \dot{T}_C - M_{\text{BMO}} c_{\text{BMO}} \dot{T}_{\text{BMO}} = Q_{\text{rad,BMO}} + Q_{\text{rad,C}} + Q_{iC} - Q_{\text{BMO}}.$$

We assume that the core and BMO cool at the same rate such that $\dot{T}_C \approx \dot{T}_{\text{BMO}}$. This assumption is justified if the more viscous solid mantle regulates the cooling rate of both reservoirs. This allows us to write

$$-\dot{T}_C (M_C c_C + M_{\text{BMO}} c_{\text{BMO}}) = Q_{\text{rad,BMO}} + Q_{\text{rad,C}} + Q_{iC} - Q_{\text{BMO}}. \quad (\text{B1})$$

The heat released at the inner core boundary is given by

$$Q_{ic} = \dot{T}_C \frac{dM_{IC}}{dT_C} (L_H + E_G), \quad (\text{B2})$$

where dM_{IC}/dT_C represents the change in inner core mass with temperature, and L_H and E_G are the latent and gravitational energy released per unit mass at the inner core boundary. Substituting into Equation (B1) yields

$$\dot{T}_C = \frac{Q_{\text{BMO}} - (Q_{\text{rad,BMO}} + Q_{\text{rad,C}})}{(M_{\text{BMO}} c_{\text{BMO}} + M_C c_C) + \frac{dM_{IC}}{dT_C} (L_H + E_G)}. \quad (\text{B3})$$

Assuming $M_{\text{BMO}} \ll M_C$, we neglect the $M_{\text{BMO}} c_{\text{BMO}}$ term in Equation (B3), yielding the final expression given in Equation (1) in Section 2.1:

$$\dot{T}_C = \frac{Q_{\text{BMO}} - Q_{\text{rad,BMO+C}}}{M_C c_C + \frac{dM_{IC}}{dT_C} (L_H + E_G)}. \quad (\text{B4})$$

B.2. Required Potassium-40 Enrichment

To estimate the required radiogenic enrichment of the BMO, we assume ^{40}K dominates the heat production. While the total BMO radiogenic heating includes contributions from ^{232}Th , ^{235}U , and ^{238}U , we approximate the calculation using ^{40}K alone – due to its short half-life, ^{40}K makes the largest contributions to radiogenic power by the end of the evolution (10 times that of ^{232}Th , 100 times that of ^{238}U , and 1000 times that of ^{235}U). Table B2 summarizes the relevant physical parameters.

Parameter	Value
Half-life ($\tau_{1/2}$)	3.942×10^{16} s
Energy per decay (E_{decay})	2.13×10^{-13} J
Atomic mass ($m_{^{40}\text{K}}$)	6.64×10^{-26} kg

Table B2. Physical parameters for ^{40}K radiogenic heating calculations.

The number of ^{40}K atoms remaining after radioactive decay over time t_{age} is given by

$$N = N_0 \exp \left(-\frac{\ln(2) \cdot t_{\text{age}}}{\tau_{1/2}} \right), \quad (\text{B5})$$

where N_0 is the initial number of atoms and $\tau_{1/2}$ is the half-life. The decay rate is related to the power output by

$$\frac{dN}{dt} = -\frac{P}{E_{\text{decay}}}, \quad (\text{B6})$$

where P is the required power (3.5 TW) and E_{decay} is the energy released per decay. Differentiating Equation (B5) with respect to time gives

$$\frac{dN}{dt} = -\frac{\ln(2)}{\tau_{1/2}} N_0 \exp\left(-\frac{\ln(2) \cdot t_{\text{age}}}{\tau_{1/2}}\right) = -\frac{\ln(2)}{\tau_{1/2}} N = -\frac{P}{E_{\text{decay}}}. \quad (\text{B7})$$

Solving for N yields

$$N = \frac{P\tau_{1/2}}{E_{\text{decay}} \ln(2)}. \quad (\text{B8})$$

Substituting $P = 3.5 \times 10^{12}$ W, $E_{\text{decay}} = 2.13 \times 10^{-13}$ J, and $\tau_{1/2} = 3.942 \times 10^{16}$ s gives $N = 5.33 \times 10^{41}$ atoms.

To determine the corresponding ^{40}K concentration in the BMO, we must specify the BMO thickness and density. We assume a BMO thickness of $L_{\text{BMO}} = 20$ km, which is in agreement with estimates of the size of ultra-low velocity zones at the core-mantle boundary (Hansen et al. 2020), and treat it as a spherical shell above the core-mantle boundary at radius $R_{\text{CMB}} = 3481$ km. Note also that the thickness of the BMO always remains smaller than the thickness of the lower boundary layer (6), so the enriched BMO never mixes into the convecting mantle. The BMO volume is

$$V_{\text{BMO}} = \frac{4\pi}{3} [(R_{\text{CMB}} + L_{\text{BMO}})^3 - R_{\text{CMB}}^3] = 3.06 \times 10^{18} \text{ m}^3. \quad (\text{B9})$$

Assuming a BMO density of $\rho_{\text{BMO}} = 6000 \text{ kg m}^{-3}$, which is slightly denser than the solid mantle due to higher pressures, the mass concentration of ^{40}K in the BMO is

$$[^{40}\text{K}]_{\text{BMO}} = \frac{Nm_{^{40}\text{K}}}{V_{\text{BMO}}\rho_{\text{BMO}}} = 3.37 \times 10^{-7}. \quad (\text{B10})$$

For comparison, we calculate the ^{40}K concentration in the solid mantle. The mantle mass is $M_{\text{man}} = M_{\oplus}f_{\text{man}} = 5.9742 \times 10^{24} \times 0.6712 = 4.01 \times 10^{24}$ kg, where f_{man} is the mantle mass fraction. Our model evolution yields a final ^{40}K mass in the mantle of 5.86×10^{16} kg, giving a concentration of

$$[^{40}\text{K}]_{\text{man}} = \frac{5.86 \times 10^{16}}{4.01 \times 10^{24}} = 1.46 \times 10^{-8}. \quad (\text{B11})$$

The enrichment factor is therefore

$$\frac{[^{40}\text{K}]_{\text{BMO}}}{[^{40}\text{K}]_{\text{man}}} = \frac{3.37 \times 10^{-7}}{1.46 \times 10^{-8}} = 23.0. \quad (\text{B12})$$

As discussed in Section 2.1, this enrichment factor of 23.0 is well within the factor of 500 allowed by Labrosse et al. (2007) for incompatible element concentration during magma ocean crystallization. This result is robust to uncertainties in BMO thickness: even if $L_{\text{BMO}} = 1$ km, the required enrichment would be ~ 463 , which is still below the theoretical upper limit. This calculation demonstrates that attributing 3.5 TW of core heating to a radiogenically enriched BMO is physically plausible and does not require extreme conditions.

REFERENCES

Abbot, D. S., Voigt, A., Li, D., et al. 2013, Journal of Geophysical Research: Atmospheres, 118, 6017

Ackerman, A. S., & Marley, M. S. 2001, The Astrophysical Journal, 556, 872

Alcubes, O. D., Olson, S., & Abbot, D. S. 2020, Monthly Notices of the Royal Astronomical Society, 492, 2572

Alfè, D., Gillan, M., & Price, G. D. 2002, Earth and Planetary Science Letters, 195, 91

Allan, R. P., Willett, K. M., John, V. O., & Trent, T. 2022, Journal of Geophysical Research: Atmospheres, 127, e2022JD036728

Appel, P. W., Rollinson, H. R., & Touret, J. L. 2001, Precambrian Research, 112, 27

Armann, M., & Tackley, P. J. 2012, *Journal of Geophysical Research: Planets*, 117

Arney, G., Domagal-Goldman, S. D., Meadows, V. S., et al. 2016, *Astrobiology*, 16, 873

Arney, G. N. 2019, *The Astrophysical Journal Letters*, 873, L7

Arney, G. N., Meadows, V. S., Domagal-Goldman, S. D., et al. 2017, *The Astrophysical Journal*, 836, 49

Atri, D., & Mogan, S. R. C. 2021, *Monthly Notices of the Royal Astronomical Society: Letters*, 500, L1

Baraffe, I., Homeier, D., Allard, F., & Chabrier, G. 2015, *Astronomy & Astrophysics*, 577, A42

Barley, M. E., Bekker, A., & Krapež, B. 2005, *Earth and Planetary Science Letters*, 238, 156

Barnes, R., Luger, R., Deitrick, R., et al. 2020, *Publications of the Astronomical Society of the Pacific*, 132, 024502

Bartman, F. L. 1980, A time variable model of earth's albedo, *Tech. rep.*, NASA

Basinger, C., Pinsonneault, M., Bastelberger, S. T., Gaudi, B. S., & Domagal-Goldman, S. D. 2024, *Monthly Notices of the Royal Astronomical Society*, 534, 2968

Batalha, N. E., Marley, M. S., Lewis, N. K., & Fortney, J. J. 2019, *The Astrophysical Journal*, 878, 70

Bercovici, D., Tackley, P., & Ricard, Y. 2015, *Treatise on Geophysics*. Elsevier, Oxford, 271

Berner, R. A. 2004, *The Phanerozoic carbon cycle: CO₂ and O₂* (Oxford University Press)

Berner, R. A., Lasaga, A. C., & Garrels, R. M. 1983, *Am. J. Sci.* (United States), 283

Bialik, O. M., Sisma-Ventura, G., Vogt-Vincent, N., Silverman, J., & Katz, T. 2022, *Scientific Reports*, 12, 15970, doi: [10.1038/s41598-022-20446-7](https://doi.org/10.1038/s41598-022-20446-7)

Blanchard, I., Siebert, J., Borensztajn, S., & Badro, J. 2017, *Geochemical Perspectives Letters*, 5, 1

Boehler, R. 1996, *Annual Review of Earth and Planetary Sciences*, 24, 15

Bouhifd, M., Gautron, L., Bofan-Casanova, N., et al. 2007, *Physics of the Earth and Planetary Interiors*, 160, 22

Boukaré, C.-É., Badro, J., & Samuel, H. 2025, *Nature*, 1

Boyd, P. W., Claustre, H., Levy, M., Siegel, D. A., & Weber, T. 2019, *Nature*, 568, 327

Boyett, M., & Carlson, R. W. 2005, *Science*, 309, 576

Brent, R. P. 2013, *Algorithms for minimization without derivatives* (Courier Corporation)

Brewer, A. 1949, *Quarterly Journal of the Royal Meteorological Society*, 75, 351

Budyko, M. I. 1969, *tellus*, 21, 611

Busse, F. H. 1976, *Physics of the Earth and Planetary Interiors*, 12, 350

Cameron, E. M., Blum, T. B., Cavosie, A. J., et al. 2024, *American Mineralogist*, 109, 1670

Campbell, I. H., & O'Neill, H. S. C. 2012, *Nature*, 483, 553

Carlson, R. W., Garnero, E., Harrison, T. M., et al. 2014, *Annual Review of Earth and Planetary Sciences*, 42, 151

Carone, L., Barnes, R., Noack, L., et al. 2025, *Astronomy & Astrophysics*, 693, A303

Carpenter, S. J., & Lohmann, K. C. 1992, *Geochimica et Cosmochimica Acta*, 56, 1837

Carroll, D., Menemenlis, D., Dutkiewicz, S., et al. 2022, *Global Biogeochemical Cycles*, 36, e2021GB007162

Catling, D. C., & Zahnle, K. J. 2009, *Scientific American*, 300, 36

—. 2020, *Science advances*, 6, eaax1420

Catling, D. C., Zahnle, K. J., & McKay, C. P. 2001, *Science*, 293, 839

Chadney, J., Galand, M., Unruh, Y., Koskinen, T., & Sanz-Forcada, J. 2015, *Icarus*, 250, 357

Chao, K.-H., deGraffenreid, R., Lach, M., et al. 2021, *Geochemistry*, 81, 125735

Charette, M. A., & Smith, W. H. 2010, *Oceanography*, 23, 112

Charnay, B., Blain, D., Bézard, B., et al. 2021, *Astronomy & Astrophysics*, 646, A171

Charnay, B., Forget, F., Wordsworth, R., et al. 2013, *Journal of Geophysical Research: Atmospheres*, 118, 10

Charnay, B., Wolf, E. T., Marty, B., & Forget, F. 2020, *Space Science Reviews*, 216, 90

Chave, K. E., & Suess, E. 1970, *Limnology and Oceanography*, 15, 633

Chidester, B. A., Lock, S., Swadba, K. E., et al. 2022, *Geochemistry, Geophysics, Geosystems*, 23, e2021GC009986

Chidester, B. A., Rahman, Z., Righter, K., & Campbell, A. J. 2017, *Geochimica et Cosmochimica Acta*, 199, 1

Chu, D. 2019, in *Remote sensing of land use and land cover in mountain region: a comprehensive study at the central Tibetan Plateau* (Springer), 195–207

Clark, R. N., Swayze, G. A., Wise, R., et al. 2003, USGS Digital Spectral Library splib05a, Open File Report 03-395, U.S. Geological Survey. <http://pubs.usgs.gov/of/2003/ofr-03-395/datable.html>

Cockell, C. S. 2014, *Philosophical Transactions of the Royal Society A: Mathematical, Physical and Engineering Sciences*, 372, 20130082

Cogley, J. G., & Henderson-Sellers, A. 1984, *Reviews of Geophysics*, 22, 131

Cogné, J.-P., & Humler, E. 2004, *Earth and Planetary Science Letters*, 227, 427

Condie, K. C., Aster, R. C., & Van Hunen, J. 2016, *Geoscience Frontiers*, 7, 543

Corgne, A., Keshav, S., Fei, Y., & McDonough, W. F. 2007, *Earth and Planetary Science Letters*, 256, 567

Crowley, J. W., Gérault, M., & O'Connell, R. J. 2011, *Earth and Planetary Science Letters*, 310, 380

de Pater, I., & Lissauer, J. 2010, *Planetary Sciences* (Cambridge University Press,)

Drugokencky, E. J., Nisbet, E. G., Fisher, R., & Lowry, D. 2011, *Philosophical Transactions of the Royal Society A: Mathematical, Physical and Engineering Sciences*, 369, 2058

Do Amaral, L. N., Barnes, R., Segura, A., & Luger, R. 2022, *The Astrophysical Journal*, 928, 12

Driscoll, P., & Bercovici, D. 2013, *Icarus*, 226, 1447

—. 2014, *Physics of the Earth and Planetary Interiors*, 236, 36

Driscoll, P., & Davies, C. 2023, *Journal of Geophysical Research: Solid Earth*, 128, e2022JB025355

Driscoll, P. E., & Barnes, R. 2015, *Astrobiology*, 15, 739

Driscoll, P. E., & Wilson, C. 2018, *Frontiers in Earth Science*, 6, 113

Eide, M., Olsen, A., Ninnemann, U. S., & Johannessen, T. 2017, *Global Biogeochemical Cycles*, 31, 515

Elkins-Tanton, L. T. 2008, *Earth and Planetary Science Letters*, 271, 181

—. 2012, *Annual Review of Earth and Planetary Sciences*, 40, 113

Etheridge, D. M., Steele, L., Langenfelds, R. L., et al. 1996, *Journal of Geophysical Research: Atmospheres*, 101, 4115

Etiope, G., & Sherwood Lollar, B. 2013, *Reviews of Geophysics*, 51, 276

Fan, S., Li, C., Li, J.-Z., et al. 2019, *The Astrophysical Journal Letters*, 882, L1

Farquhar, J., Zerkle, A. L., & Bekker, A. 2011, *Photosynthesis research*, 107, 11

Fauchez, T., Arney, G., Kopparapu, R. K., & Goldman, S. D. 2018, arXiv preprint arXiv:1811.10759

Fauchez, T. J., Turbet, M., Villanueva, G. L., et al. 2019, *The Astrophysical Journal*, 887, 194

Feely, R. A., Sabine, C. L., Takahashi, T., Wanninkhof, R., et al. 2001, *Oceanography*, 14, 18

Feinberg, L. D., Sitarski, B. N., McElwain, M. W., et al. 2026, *Habitable Worlds Observatory's Concept and Technology Maturation: Initial Feasibility and Trade Space Exploration*. <https://arxiv.org/abs/2601.11803>

Feulner, G. 2012, *Reviews of Geophysics*, 50

Fischer, T. P. 2008, *Geochemical Journal*, 42, 21

Fleming, J. R. 1998, *Historical perspectives on climate change* (Oxford University Press)

Foley, B. J. 2015, *The Astrophysical Journal*, 812, 36

—. 2019, *The Astrophysical Journal*, 875, 72

Foley, B. J., & Driscoll, P. E. 2016, *Geochemistry, Geophysics, Geosystems*, 17, 1885

Foley, B. J., & Smye, A. J. 2018, *Astrobiology*, 18, 873

Foriel, J., Philippot, P., Rey, P., et al. 2004, *Earth and Planetary Science Letters*, 228, 451

Frank, E. A., Meyer, B. S., & Mojzsis, S. J. 2014, *Icarus*, 243, 274

Gaillard, F., Bernadou, F., Roskosz, M., et al. 2022, *Earth and Planetary Science Letters*, 577, 117255

Gale, A., Dalton, C. A., Langmuir, C. H., Su, Y., & Schilling, J.-G. 2013, *Geochemistry, Geophysics, Geosystems*, 14, 489

Garcia, R., Barnes, R. K., Driscoll, P. E., Gialluca, M. T., & Meadows, V. S. 2026, *The Planetary Science Journal*, submitted

Gebauer, S., Grenfell, J., Stock, J. W., et al. 2017, *Astrobiology*, 17, 27

Genda, H. 2016, *Geochemical Journal*, 50, 27

Gérard, J.-C., Hauglustaine, D. A., & François, L. 1992, *Palaeogeography, Palaeoclimatology, Palaeoecology*, 97, 133

Gialluca, M. T., Barnes, R., Meadows, V. S., et al. 2024, *The Planetary Science Journal*, 5, 137

Gillmann, C., Way, M. J., Avice, G., et al. 2022, *Space Science Reviews*, 218, 56

Godolt, M., Grenfell, J., Kitzmann, D., et al. 2016, *Astronomy & Astrophysics*, 592, A36

Godolt, M., Grenfell, J., Hamann-Reinus, A., et al. 2015, *Planetary and Space Science*, 111, 62

Goldblatt, C., Claire, M. W., Lenton, T. M., et al. 2009, *Nature Geoscience*, 2, 891

Goldblatt, C., & Zahnle, K. J. 2011, *Nature*, 474, E1

Gordon, I. E., Rothman, L. S., Hill, C., et al. 2017, *Journal of quantitative spectroscopy and radiative transfer*, 203, 3

Gough, D. 1981, *Solar Physics*, 74, 21

Gronoff, G., Arras, P., Baraka, S., et al. 2020, *Journal of Geophysical Research: Space Physics*, 125, e2019JA027639

Grotzinger, J. P. 1989, *SEPM Special Publication*, 44, 79

Grotzinger, J. P., & James, N. P. 2000, in *Carbonate Sedimentation and Diagenesis in the Evolving Precambrian World*, ed. J. P. Grotzinger & N. P. James (SEPM Society for Sedimentary Geology), 3–20

Grotzinger, J. P., & Kasting, J. F. 1993, *Journal of Geology*, 101, 235, doi: [10.1086/648218](https://doi.org/10.1086/648218)

Gunell, H., Maggioli, R., Nilsson, H., et al. 2018, *Astronomy & Astrophysics*, 614, L3

Halevy, I., & Bachan, A. 2017, *Science*, 355, 1069

Hansen, S. E., Carson, S. E., Garnero, E. J., Rost, S., & Yu, S. 2020, *Earth and Planetary Science Letters*, 536, 116142

Haqq-Misra, J. D., Domagal-Goldman, S. D., Kasting, P. J., & Kasting, J. F. 2008, *Astrobiology*, 8, 1127

Harrison, E. F., Minnis, P., Barkstrom, B., et al. 1990, *Journal of Geophysical Research: Atmospheres*, 95, 18687

Hashimoto, G. L., & Abe, Y. 2001, *Journal of Geophysical Research: Planets*, 106, 14675

Hawkins, E., & Sutton, R. 2016, *Bulletin of the American Meteorological Society*, 97, 963

Hawkins, E., Ortega, P., Suckling, E., et al. 2017, *Bulletin of the American Meteorological Society*, 98, 1841

Held, I. M., & Soden, B. J. 2000, *Annual review of energy and the environment*, 25, 441

Helling, C. 2019, *Annual Review of Earth and Planetary Sciences*, 47, 583

Herzberg, C., Condie, K., & Korenaga, J. 2010, *Earth and Planetary Science Letters*, 292, 79

Hirao, N., Ohtani, E., Kondo, T., et al. 2006, *Geophysical Research Letters*, 33

Hirose, K., Labrosse, S., & Hernlund, J. 2013, *Annual Review of Earth and Planetary Sciences*, 41, 657

Hoffman, P. F., Abbot, D. S., Ashkenazy, Y., et al. 2017, *Science Advances*, 3, e1600983

Holland, H. D. 2020, *The chemical evolution of the atmosphere and oceans* (Princeton University Press)

Jackson, M. G., Carlson, R. W., Kurz, M. D., et al. 2010, *Nature*, 466, 853

Jaupart, C., Labrosse, S., Lucaleau, F., & Mareschal, J. 2015, *Treatise on geophysics. Temperatures, heat and energy in the mantle of the Earth*, Elsevier, Oxford

Jeanloz, R., & Morris, S. 1986, IN: *Annual review of earth and planetary sciences. Volume 14 (A87-13190 03-46)*. Palo Alto, CA, Annual Reviews, Inc., 1986, p. 377-415. NSF-NASA-supported research., 14, 377

Jenkins, G. S. 1993, *Journal of Geophysical Research: Atmospheres*, 98, 20803

—. 1995a, *Geophysical research letters*, 22, 1513

—. 1995b, *Geophysical Research Letters*, 22, 2077

—. 1999, *Global and Planetary Change*, 20, 257

Jet Propulsion Laboratory. 1999, *ASTER Spectral Library*. <http://speclib.jpl.nasa.gov>

Jiang, L.-Q., Carter, B. R., Feely, R. A., Lauvset, S. K., & Olsen, A. 2019, *Scientific reports*, 9, 18624

Jones, E., Oliphant, T., Peterson, P., et al. 2001, *SciPy: Open source scientific tools for Python*, <https://www.scipy.org>

Kaltenegger, L., Traub, W. A., & Jucks, K. W. 2007, *The Astrophysical Journal*, 658, 598

Kargel, J. S., Leonard, G. J., Bishop, M. P., Kääb, A., & Raup, B. H. 2014, *Global land ice measurements from space* (Springer)

Kasting, J. F. 1987, *Precambrian research*, 34, 205

—. 1988, *Icarus*, 74, 472

—. 2010, *Nature*, 464, 687

Kasting, J. F., & Catling, D. 2003, *Annual Review of Astronomy and Astrophysics*, 41, 429

Kasting, J. F., Whitmire, D. P., & Reynolds, R. T. 1993, *Icarus*, 101, 108

Katsura, T., Yamada, H., Shinmei, T., et al. 2003, *Physics of the Earth and Planetary Interiors*, 136, 11

Katsura, T., Yamada, H., Nishikawa, O., et al. 2004, *Journal of Geophysical Research: Solid Earth*, 109

Kerrick, D. M. 2001, *Reviews of Geophysics*, 39, 565

Kharecha, P., Kasting, J., & Siefert, J. 2005, *Geobiology*, 3, 53

Kinzler, R. J., & Grove, T. L. 1992, *Journal of Geophysical Research: Solid Earth*, 97, 6885

Kipping, D. 2025, *Astrobiology*, 25, 323

Kirchner, J. W. 1989, *Reviews of Geophysics*, 27, 223

—. 2002, *Climatic change*, 52, 391

—. 2003, *Climatic Change*, 58, 21

Kivelson, M. G., & Bagenal, F. 2014, in *Encyclopedia of the solar system* (Elsevier), 137–157

Klein, E. M., & Langmuir, C. H. 1987, *Journal of Geophysical Research: Solid Earth*, 92, 8089

Knauth, L. P., & Epstein, S. 1976, *Geochimica et Cosmochimica Acta*, 40, 1095

Knauth, L. P., & Lowe, D. R. 2003, *Geological Society of America Bulletin*, 115, 566

Komacek, T. D., & Abbot, D. S. 2019, *The Astrophysical Journal*, 871, 245

Konôpková, Z., McWilliams, R. S., Gómez-Pérez, N., & Goncharov, A. F. 2016, *Nature*, 534, 99

Kopparapu, R. K., Ramirez, R., Kasting, J. F., et al. 2013, *The Astrophysical Journal*, 765, 131

Korenaga, J. 2018, *Philosophical Transactions of the Royal Society A: Mathematical, Physical and Engineering Sciences*, 376, 20170408

Krissansen-Totton, J., Arney, G. N., & Catling, D. C. 2018, *Proceedings of the National Academy of Sciences*, 115, 4105

Krissansen-Totton, J., Fortney, J. J., Nimmo, F., & Wogan, N. 2021, *AGU Advances*, 2, e2020AV000294

Kump, L. R. 2008, *Nature*, 451, 277

Labrosse, S. 2003, *Physics of the Earth and Planetary Interiors*, 140, 127

Labrosse, S., Hernlund, J., & Coltice, N. 2007, *Nature*, 450, 866

Lammer, H., Zerkle, A. L., Gebauer, S., et al. 2018, *The Astronomy and Astrophysics Review*, 26, 2

Laneuville, M., Kameya, M., & Cleaves, H. J. 2018, *Astrobiology*, 18, 897

Le Moigne, F. A. 2019, *Frontiers in Marine Science*, 6, 634

Leconte, J., Forget, F., Charnay, B., et al. 2013, *Astronomy & Astrophysics*, 554, A69

Lee, C.-T. A., Luffi, P., Höink, T., et al. 2010, *Nature*, 463, 930

Li, J., Jian, H., Chen, Y. J., et al. 2015, *Geophysical Research Letters*, 42, 2656

Lichtenberg, T., Bower, D. J., Hammond, M., et al. 2021, *Journal of Geophysical Research: Planets*, 126, e2020JE006711

Lincowski, A. P., Meadows, V. S., Crisp, D., et al. 2018, *The Astrophysical Journal*, 867, 76

Loeb, N. G., Wielicki, B. A., Doelling, D. R., et al. 2009, *Journal of Climate*, 22, 748

López-Morales, M., Currie, T., Teske, J., et al. 2019, arXiv preprint arXiv:1903.09523

Lovelock, J. 2000, *The ages of Gaia: A biography of our living earth* (Oxford University Press, USA)

—. 2016, *Gaia: A new look at life on earth* (Oxford University Press)

Lovelock, J. E. 1983, in *Biomineralization and biological metal accumulation: biological and geological perspectives* papers presented at the fourth international symposium on biominerization, renesse, The Netherlands, june 2–5, 1982, Springer, 15–25

Lovelock, J. E., & Margulis, L. 1974, *Tellus*, 26, 2

Luger, R., & Barnes, R. 2015, *Astrobiology*, 15, 119

Lustig-Yaeger, J., Meadows, V. S., Crisp, D., Line, M. R., & Robinson, T. D. 2023, *The Planetary Science Journal*, 4, 170

Lyons, T. W., Reinhard, C. T., & Planavsky, N. J. 2014, *Nature*, 506, 307

Mamajek, E., & Stapelfeldt, K. 2023, *NASA ExEP Mission Star List for the Habitable Worlds Observatory*, Tech. rep., NASA Jet Propulsion Laboratory and California Institute of Technology

Marty, B., Zimmermann, L., Pujol, M., Burgess, R., & Philippot, P. 2013, *Science*, 342, 101

Mauritsen, T., Stevens, B., Roeckner, E., et al. 2012, *Journal of advances in modeling Earth systems*, 4

McCollom, T. M. 2003, *Geochimica et Cosmochimica Acta*, 67, 311

—. 2016, *Proceedings of the National Academy of Sciences*, 113, 13965

Meadows, V. S., & Crisp, D. 1996, *Journal of Geophysical Research: Planets*, 101, 4595

Meadows, V. S., Reinhard, C. T., Arney, G. N., et al. 2018, *Astrobiology*, 18, 630

Millero, F. J. 2005, *Chemical oceanography*, Vol. 30 (CRC press)

Mockler, S. 1995, *Special Report*, American, Geophysical Union

Mojzsis, S. J., Harrison, T. M., & Pidgeon, R. T. 2001, *Nature*, 409, 178

Molnar, G. I., & Gutowski Jr, W. J. 1995, *Journal of Glaciology*, 41, 87

Nakagawa, T., & Tackley, P. J. 2012, *Earth and Planetary Science Letters*, 329, 1

National Academies of Sciences, Engineering, and Medicine. 2021, *Pathways to Discovery in Astronomy and Astrophysics for the 2020s* (The National Academies Press)

Nelder, J. A., & Mead, R. 1965, *The Computer Journal*, 7, 308, doi: [10.1093/comjnl/7.4.308](https://doi.org/10.1093/comjnl/7.4.308)

Newman, M. J., & Rood, R. T. 1977, *Science*, 198, 1035

Nicholson, A. E., Wilkinson, D. M., Williams, H. T., & Lenton, T. M. 2018, *Monthly Notices of the Royal Astronomical Society*, 477, 727

Nikolaou, A., Katyal, N., Tosi, N., et al. 2019, *The Astrophysical Journal*, 875, 11

Nimmo, F. 2002, *Geology*, 30, 987

North, G. R. 2024, *Current Opinion in Chemical Engineering*, 44, 101010

North, G. R., & Coakley Jr, J. A. 1979, *Journal of Atmospheric Sciences*, 36, 1189

Nowicki, M., DeVries, T., & Siegel, D. A. 2022, *Global Biogeochemical Cycles*, 36, e2021GB007083

Ohta, K., Kuwayama, Y., Hirose, K., Shimizu, K., & Ohishi, Y. 2016, *Nature*, 534, 95

O'Leary, M. H. 1981, *Phytochemistry*, 20, 553

Olson, P., & Christensen, U. R. 2006, *Earth and Planetary Science Letters*, 250, 561

Passow, U., & Carlson, C. A. 2012, *Marine Ecology Progress Series*, 470, 249, doi: [10.3354/meps09985](https://doi.org/10.3354/meps09985)

Patel, V. K., & Kuttippurath, J. 2023, *Ocean-Land-Atmosphere Research*, 2, 0015

Paulson, A., Zhong, S., & Wahr, J. 2005, *Geophysical Journal International*, 163, 357

Pavlov, A. A., Brown, L. L., & Kasting, J. F. 2001, *Journal of Geophysical Research: Planets*, 106, 23267

Pavlov, A. A., Kasting, J. F., Brown, L. L., Rages, K. A., & Freedman, R. 2000, *Journal of Geophysical Research: Planets*, 105, 11981

Pilson, M. E. 2012, *An Introduction to the Chemistry of the Sea* (cambridge university press)

Pozzo, M., Davies, C. J., & Alfe, D. 2022, *Earth and Planetary Science Letters*, 584, 117466

Quay, P., Sonnerup, R., Westby, T., Stutsman, J., & McNichol, A. 2003, *Global Biogeochemical Cycles*, 17, 4

Ramanathan, V., Cess, R., Harrison, E., et al. 1989, *Science*, 243, 57

Randel, W., & Park, M. 2019, *Journal of Geophysical Research: Atmospheres*, 124, 7018

Ray, R. D., Eanes, R., & Chao, B. F. 1996, *Nature*, 381, 595

Roberson, A. L., Roadt, J., Halevy, I., & Kasting, J. 2011, *Geobiology*, 9, 313

Robinson, T. D., Meadows, V. S., Crisp, D., et al. 2011, *Astrobiology*, 11, 393

Rodler, F., & López-Morales, M. 2014, *The Astrophysical Journal*, 781, 54

Rose, B. E., Cronin, T. W., & Bitz, C. M. 2017, *The Astrophysical Journal*, 846, 28

Rosing, M. T., Bird, D. K., Sleep, N. H., & Bjerrum, C. J. 2010, *Nature*, 464, 744

Rothman, L. S., Gordon, I., Barber, R., et al. 2010, *Journal of Quantitative Spectroscopy and Radiative Transfer*, 111, 2139

Rugheimer, S., & Kaltenegger, L. 2018, *The Astrophysical Journal*, 854, 19

Sagan, C., & Mullen, G. 1972, *Science*, 177, 52

Sandu, C., Lenardic, A., & McGovern, P. 2011, *Journal of Geophysical Research: Solid Earth*, 116

Santerne, A., Brugger, B., Armstrong, D., et al. 2018, *Nature Astronomy*, 2, 393

Saunois, M., Stavert, A. R., Poulter, B., et al. 2019, *Earth System Science Data Discussions*, 2019, 1

Schaefer, L., & Elkins-Tanton, L. T. 2018, *Philosophical Transactions of the Royal Society A: Mathematical, Physical and Engineering Sciences*, 376, 20180109

Schaefer, L., & Sasselov, D. 2015, *The Astrophysical Journal*, 801, 40

Schaefer, L., Wordsworth, R. D., Berta-Thompson, Z., & Sasselov, D. 2016, *The Astrophysical Journal*, 829, 63

Schatten, K. H., & Endal, A. S. 1982, *Geophysical Research Letters*, 9, 1309

Schieterman, E. W., Reinhard, C. T., Olson, S. L., Harman, C. E., & Lyons, T. W. 2019a, *The Astrophysical Journal*, 878, 19

Schieterman, E. W., Reinhard, C. T., Olson, S. L., et al. 2019b, *The Astrophysical Journal*, 874, 9

Schieterman, E. W., Robinson, T. D., Meadows, V. S., Misra, A., & Domagal-Goldman, S. 2015, *The Astrophysical Journal*, 810, 57

Schieterman, E. W., Kiang, N. Y., Parenteau, M. N., et al. 2018, *Astrobiology*, 18, 663

Seales, J., & Lenardic, A. 2020, *Geochemistry, Geophysics, Geosystems*, 21, e2020GC009106

Segura, A., Kasting, J. F., Meadows, V., et al. 2005, *Astrobiology*, 5, 706

Segura, A., Walkowicz, L. M., Meadows, V., Kasting, J., & Hawley, S. 2010, *Astrobiology*, 10, 751

Sellers, W. D. 1969, *Journal of Applied Meteorology* (1962-1982), 392

Shaik, I., Nagamani, P., Yadav, S., Manmode, Y., & Rao, G. S. 2025, *Marine Chemistry*, 268, 104483

Shim, S.-H. 2014, *Search for Life Beyond the Solar System. Exoplanets, Biosignatures & Instruments*, 2

Siegel, D. A., DeVries, T., Cetinić, I., & Bisson, K. M. 2023, *Annual review of marine science*, 15, 329

Sleep, N. H., & Zahnle, K. 2001, *Journal of Geophysical Research: Planets*, 106, 1373

Solomon, S., Qin, D., Manning, M., et al. 2007, *Climate change*, 374

Som, S. M., Buick, R., Hagadorn, J. W., et al. 2016, *Nature Geoscience*, 9, 448

Som, S. M., Catling, D. C., Harnmeijer, J. P., Polivka, P. M., & Buick, R. 2012, *Nature*, 484, 359

Spohn, T., & Breuer, D. 2016, in *EGU General Assembly Conference Abstracts*, EPSC2016-18377

Stalport, F., Coll, P., Cabane, M., et al. 2005, *Geophysical Research Letters*, 32

Stueken, E. E., Som, S., Claire, M., et al. 2020, *Space Science Reviews*, 216, 31

Sumner, D. Y., & Grotzinger, J. P. 1996, *Geology*, 24, 119, doi: [10.1130/0091-7613\(1996\)024\(0119:WKOACC\)2.3.CO;2](https://doi.org/10.1130/0091-7613(1996)024(0119:WKOACC)2.3.CO;2)

Tartèse, R., Chaussidon, M., Gurenko, A., et al. 2016, *Geochemical Perspectives Letters*, 3, 55

Thompson, M. A., Krissansen-Totton, J., Wogan, N., Telus, M., & Fortney, J. J. 2022, *Proceedings of the National Academy of Sciences*, 119, e2117933119

Tian, F., Chassefière, E., Leblanc, F., & Brain, D. 2013, *Comparative climatology of terrestrial planets*, chapitre

Tolstikhin, I., & Hofmann, A. W. 2005, *Physics of the Earth and Planetary Interiors*, 148, 109

Toon, O. B., McKay, C., Ackerman, T., & Santhanam, K. 1989, *Journal of Geophysical Research: Atmospheres*, 94, 16287

Trenberth, K. E., Christy, J. R., & Olson, J. G. 1987, *Journal of Geophysical Research: Atmospheres*, 92, 14815

Tsigaridis, K., Ackerman, A. S., Aleinov, I., et al. 2025, *EGUphere*, 2025,

Tuchow, N. W., Harada, C. K., Mamajek, E. E., et al. 2025, *Publications of the Astronomical Society of the Pacific*, 137, 104402

Turbet, M., Bolmont, E., Leconte, J., et al. 2018, *Astronomy & Astrophysics*, 612, A86

Tyndall, J. 1861, *The London, Edinburgh, and Dublin Philosophical Magazine and Journal of Science*, 22, 169

United States Committee on Extension to the Standard Atmosphere. 1976, *US standard atmosphere*, 1976 (National Oceanic and Atmospheric Administration)

Vial, J., Dufresne, J.-L., & Bony, S. 2013, *Climate Dynamics*, 41, 3339

Virtanen, P., Gommers, R., Oliphant, T. E., et al. 2019, arXiv e-prints, arXiv:1907.10121. <https://arxiv.org/abs/1907.10121>

Virtanen, P., Gommers, R., Oliphant, T. E., et al. 2020, *Nature Methods*, 17, 261, doi: [10.1038/s41592-019-0686-2](https://doi.org/10.1038/s41592-019-0686-2)

Vladilo, G., Murante, G., Silva, L., et al. 2013, *The Astrophysical Journal*, 767, 65

Volk, T. 2002, *Climatic Change*, 52, 423

Walker, J. C., Hays, P., & Kasting, J. F. 1981, *Journal of Geophysical Research: Oceans*, 86, 9776

Walter, M., Buick, R., & Dunlop, J. 1980, *Nature*, 284, 443

Wang, Z., Zhang, J., Zong, K., Kusky, T. M., & Wang, Y. 2023, *Journal of Earth Science*, 34, 1645

Watanabe, K., Ohtani, E., Kamada, S., et al. 2014, *Physics of the Earth and Planetary Interiors*, 237, 65

Watson, A. J., Donahue, T. M., & Walker, J. C. 1981, *Icarus*, 48, 150

Way, M. J., Del Genio, A. D., Aleinov, I., et al. 2018, *The Astrophysical Journal Supplement Series*, 239, 24

Way, M. J., Aleinov, I., Amundsen, D. S., et al. 2017, *The Astrophysical Journal Supplement Series*, 231, 12

Wielicki, B. A., Barkstrom, B. R., Harrison, E. F., et al. 1996, *Bulletin of the American Meteorological Society*, 77, 853

Wilde, S. A., Valley, J. W., Peck, W. H., & Graham, C. M. 2001, *Nature*, 409, 175

Wilhelm, C., Barnes, R., Deitrick, R., & Mellman, R. 2022, *The Planetary Science Journal*, 3, 13

Windsor, J. D., Robinson, T. D., kumar Kopparapu, R., et al. 2023, *The Planetary Science Journal*, 4, 94

Winterhalder, T., Lacour, S., Mérand, A., et al. 2024, *Astronomy & Astrophysics*, 688, A44

Wogan, N., Krissansen-Totton, J., & Catling, D. C. 2020, *The Planetary Science Journal*, 1, 58

Wogan, N., Lopez, J., Batalha, N., & Fortney, J. 2025a, Resampled Opacity Databases for PICASO from the Photochem model, v1.0.0, Zenodo, doi: [10.5281/zenodo.1738117](https://doi.org/10.5281/zenodo.1738117)

Wogan, N. F., Catling, D. C., Zahnle, K. J., & Claire, M. W. 2022, *Proceedings of the National Academy of Sciences*, 119, e2205618119

Wogan, N. F., Batalha, N. E., Zahnle, K., et al. 2025b, *The Planetary Science Journal*, 6, 256

Wolf, E. T., Kopparapu, R., Haqq-Misra, J., & Fauchez, T. J. 2022, *The Planetary Science Journal*, 3, 7

Wolf, E. T., Shields, A. L., Kopparapu, R. K., Haqq-Misra, J., & Toon, O. B. 2017, *The Astrophysical Journal*, 837, 107

Wordsworth, R., & Pierrehumbert, R. 2014, *The Astrophysical Journal Letters*, 785, L20

Xiong, Z., Tsuchiya, T., & Taniuchi, T. 2018, *Journal of Geophysical Research: Solid Earth*, 123, 6451

Yang, J., Leconte, J., Wolf, E. T., et al. 2016, *The Astrophysical Journal*, 826, 222

Young, A. V., Robinson, T. D., Krissansen-Totton, J., et al. 2023, arXiv preprint arXiv:2311.06083

Zahnle, K. J., Gacesa, M., & Catling, D. C. 2019, *Geochimica et Cosmochimica Acta*, 244, 56

Zahnle, K. J., Lupu, R., Catling, D. C., & Wogan, N. 2020, *The Planetary Science Journal*, 1, 11

Zerkle, A. L., Claire, M. W., Domagal-Goldman, S. D., Farquhar, J., & Poulton, S. W. 2012, *Nature Geoscience*, 5, 359

Zhuang, D., Yan, H., Tucker, M. E., et al. 2018, *Chemical Geology*, 500, 64

Zsom, A., Kaltenegger, L., & Goldblatt, C. 2012, *Icarus*, 221, 603